Synthesis of MgAl2O4 by sol-gel method and investigation of catalytic performances in CO2 methanation

Downloaded from: https://research.chalmers.se, 2026-01-21 13:58 UTC

Citation for the original published paper (version of record):
Yeşiltepe-Özçelik, D., Burgun, U., Kaya, F. et al (2025). Synthesis of MgAl2O4 by sol-gel method and investigation of catalytic performances in CO2 methanation. Journal of Sol-Gel Science and Technology, 116(1): 634-655. http://dx.doi.org/10.1007/s10971-025-06799-1

N.B. When citing this work, cite the original published paper.

research.chalmers.se offers the possibility of retrieving research publications produced at Chalmers University of Technology. It covers all kind of research output: articles, dissertations, conference papers, reports etc. since 2004. research.chalmers.se is administrated and maintained by Chalmers Library

(article starts on next page)

Journal of Sol-Gel Science and Technology (2025) 116:634–655
https://doi.org/10.1007/s10971-025-06799-1

ORIGINAL PAPER

Synthesis of $MgAl_2O_4$ by sol-gel method and investigation of catalytic performances in CO_2 methanation

Duygu Yeşiltepe-Özçelik[1,2] · Utku Burgun[3,4] · Faruk Kaya[1] · Emircan Uysal[1] · Bora Derin[1] · Andreas Schaefer[5,6] · Per-Anders Carlsson[5,6] · Gamze Gümüşlü-Gür[3,4] · Alper Sarıoğlan[3,4] · Sebahattin Gürmen[1]

Received: 29 December 2024 / Accepted: 10 May 2025 / Published online: 23 May 2025
© The Author(s) 2025

Abstract

CO_2 levels in the atmosphere are increasing as a result of human activities such as industrial activities, fossil fuel usage, and deforestation. The CO_2 methanation reaction, which converts CO_2 into methane, may play a crucial role in addressing this issue. Like most commercial syntheses, the CO_2 methanation process requires a catalyst. Spinel catalysts, particularly magnesium aluminate ($MgAl_2O_4$), have gained attention for their potential in CO_2 methanation. In this study, $MgAl_2O_4$ nanoparticles were synthesized using a sol–gel method with a molar ratio of Mg:Al = 1:2, and calcined at temperatures ranging from 700 to 900 °C. The structural properties of the nanoparticles were characterized using differential scanning calorimetry, thermogravimetric analysis, Fourier transform infrared spectroscopy, Brunauer-Emmett-Teller analysis, X-ray diffraction, field emission scanning electron microscopy, energy dispersive X-ray spectroscopy, and transmission electron microscopy. The results showed that the particles had nearly spherical morphology, with agglomeration occurring at higher temperatures. The surface area decreased with increasing calcination temperature, from 188 m²/g at 700 °C to 94 m²/g at 900 °C. NiCo-$MgAl_2O_4$ catalysts were prepared by impregnation and characterized by CO_2 temperature-programmed desorption and hydrogen temperature-programmed reduction. Catalytic performance tests revealed that the NiCo-$MgAl_2O_4$ catalyst calcined at 800 °C achieved the highest CO_2 conversion (~85%) and methane selectivity. Spent catalyst analysis showed that carbon deposition negatively affected catalyst performance over time. This study emphasizes the role of strong basic sites in CO_2 activation and methane formation, suggesting future improvements in catalyst stability.

Graphical Abstract

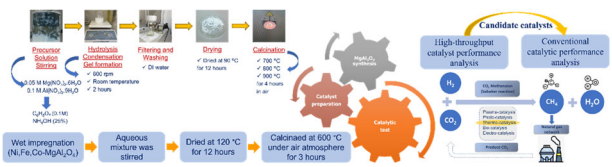

Keywords $MgAl_2O_4$ · sol-gel · CO_2 methanation · Ni-Co · CO_2 conversion · CH_4 selectivity

✉ Duygu Yeşiltepe-Özçelik
yesiltepe15@itu.edu.tr

[1] Department of Metallurgical and Materials Engineering, Istanbul Technical University, Istanbul, Turkey

[2] Department of Mechanical Engineering, Osmaniye Korkut Ata University, Osmaniye, Turkey

[3] Department of Chemical Engineering, Istanbul Technical University, Istanbul, Turkey

[4] ITU Synthetic Fuels and Chemicals Technology Center, ITU-SENTEK, Istanbul Technical University, Istanbul, Turkey

[5] Department of Chemistry and Chemical Engineering, Chalmers University of Technology, Gothenburg, Sweden

[6] Competence Centre for Catalysis, Chalmers University of Technology, Gothenburg, Sweden

Highlights

- $MgAl_2O_4$ nanoparticles were synthesized via a sol-gel method.
- Rietveld analysis shows $MgAl_2O_4$ adopts cubic Fd-3m space group with a lattice parameter of 8.0546 Å.
- The effect of active metals (Ni, Fe, Co) on catalytic performance was studied.
- The calcination temperature of the support significantly influenced the catalytic properties.
- Ni-Co/$MgAl_2O_4$ catalysts showed excellent CO_2 conversion (~85%) and CH_4 selectivity.

1 Introduction

Carbon dioxide (CO_2) concentrations in the atmosphere have been rising steadily due to human activities such as industrialization, excessive fossil fuel usage, and deforestation. As of 2024, atmospheric CO_2 levels have reached 425 parts per million (ppm) [1]. Scientists indicate that the increase in CO_2 and other greenhouse gases intensifies global warming and climate change [1, 2]. According to the Intergovernmental Panel on Climate Change (IPCC) 2023 report, limiting global warming to 1.5 °C requires rapid and deep reductions in greenhouse gas emissions across all sectors, aiming for net zero CO_2 emissions by the early 2050 s [3–5]. This imperative highlights the urgent need for innovative and scalable strategies to mitigate carbon emissions.

Carbon Capture Utilization and Storage (CCUS) technologies are expected to be an effective means of achieving carbon neutrality in this context, and the circular CO_2 economy is essential for decarbonization [6]. Using CO_2 as a feedstock to produce value-added fuels and chemicals provides a workable solution to reduce greenhouse gas emissions in the atmosphere. Specifically, the hydrogenation of CO_2 using green hydrogen (H_2)–derived from renewable energy sources–offers a sustainable and economical pathway for converting CO_2 into valuable products while minimizing environmental impact. Nevertheless, most CCUS processes face challenges such as high energy requirements due to severe operational conditions or low equilibrium conversions caused by the strong thermodynamic stability of CO_2 [7]. Among these pathways, the methanation reaction, also known as the Sabatier reaction, has gained significant attention for its potential in Power-to-Gas technology and biogas upgrading. Originally employed to remove trace CO_2 during ammonia (NH_3) production, CO_2 methanation enables the conversion of CO_2 and surplus renewable H_2 into methane (CH_4), facilitating the storage and transport of renewable energy via existing natural gas infrastructure [8]. CO_2 methanation can be seen as a direct reaction (Rxn. 1) or as a combination of Reverse Water-Gas Shift (RWGS) (Rxn. 2) and CO methanation (Rxn. 3). CO evolution alongside methane may occur since RWGS and CO_2 methanation requires the same reactants. Since the overall reaction is promoted at low temperature and high pressure according to Le Chatelier's principle, it is crucial to utilize an active catalyst to overcome kinetic constraints and enhance reaction rates [9–11].

$$CO_{2(g)} + 4\,H_{2(g)} \rightleftharpoons CH_{4(g)} + 2H_2O_{(g)}\ \Delta H_{298K,1atm} = -165.4\,kJ/mol \quad (1)$$

$$CO_{2(g)} + H_{2(g)} \rightleftharpoons CO_{(g)} + H_2O_{(g)}\ \Delta H_{298K,1atm} = 41.17\,kJ/mol \quad (2)$$

$$CO_{(g)} + 3\,H_{2(g)} \rightleftharpoons CH_{4(g)} + H_2O_{(g)}\ \Delta H_{298K,1atm} = -206.3\,kJ/mol \quad (3)$$

This study focuses on optimizing these reactions at 350 °C, where side reactions are minimized. Spinel catalysts, with their distinctive AB_2O_4 structure, have gained attention for CO_2 methanation due to their flexibility in composition and structural properties. This adaptability allows for the fine-tuning of catalytic performance, particularly through modifications with active metals like nickel (Ni) and additives such as manganese (Mn), to enhance activity and stability while minimizing by product formation [1, 2, 4, 12]. Ni-based spinel catalysts, in particular, have shown promising results for CO_2 methanation, offering high catalytic efficiency through improved dispersion of active sites and stabilization of reactive intermediates [13]. Support materials play a critical role in heterogeneous catalysis, influencing both activity and selectivity. Therefore, utilizing spinel-based supports to provide favorable textural properties, including a high surface area for the dispersion of active species and a pore structure that would facilitates reactant diffusion, is essential [14].

The characteristics of spinel-structured catalysts-such as their high surface area, controlled porosity, and defect sites-facilitate efficient gas-phase reactions and accelerate CO_2 bond activation. For instance, in the $MgAl_2O_4$ (MA) spinel structure with insufficient sites (Mg/Al <1/2), Ni predominantly occupies the A-site of MA, which fixates Ni in catalytically active configurations and has a high potential for enhancing CO_2 methanation efficiency [15]. The use of noble metals (e.g., ruthenium (Ru), rhodium (Rh), palladium (Pd)), as well as rare-earth oxides (e.g., cerium oxide (CeO_2)), is well-documented in CO_2 methanation reactions due to their remarkable activity and selectivity [11, 16–20]. Titanium dioxide (TiO_2) is another widely used material for

its high surface area and chemical stability [21]. However, the high cost and limited availability of these materials pose significant challenges for large-scale industrial applications. For example, while CeO_2 and TiO_2 demonstrate good catalytic properties, they have limitations such as lower oxygen storage capacity compared to spinel structures like MA, susceptibility to phase changes (in the case of TiO_2), and higher costs [19, 21]. These challenges necessitate the development of cost-effective alternatives that maintain high catalytic performance.

Nickel (Ni) and cobalt (Co)-based catalysts have emerged as promising alternatives due to their lower cost, abundant availability, and established catalytic performance in CO_2 methanation [20–26]. In this study, the NiCo-MA catalyst was selected as an economical and sustainable alternative to noble metal, rare-earth, and titanium-based systems. The MA spinel structure offers unique advantages, including high thermal stability, mechanical robustness, and enhanced dispersion of active metal phases, which help mitigate sintering and carbon deposition. Additionally, the presence of deficient sites in the MA structure provides favorable conditions for the stabilization of active metals like Ni, which predominantly occupies the A-site, further enhancing catalytic performance. These attributes make the NiCo-MA catalyst a viable candidate for scalable and sustainable industrial applications.

This study explores the development of MA supported Ni, NiFe and NiCo catalysts for low-temperature CO_2 methanation, aiming to overcome current limitations such as kinetic barriers, coke formation, and catalyst deactivation. Our approach focuses on optimizing the spinel structure through sol-gel synthesis and targeted metal impregnation to achieve high activity and selectivity at 350 °C and 1 atm pressure. While significant advancements have been made in catalyst design, further studies are required to fully understand the effects of preparation methods, calcination temperatures, and structural features on catalytic performance. These factors are crucial for controlling the interaction between active metals and the support, directly impacting catalytic activity, stability, and resistance to deactivation.

In this work, the sol-gel method was used for the production of spinel support materials due to its distinct advantages over alternative production methods. The sol-gel process operates at lower temperatures than high-temperature solid-state techniques, providing enhanced control over the particle size, shape, and composition [27–29]. This control is crucial for optimizing catalytic performance, as smaller particles and more homogeneous structures often lead to higher catalytic activity [30–32]. Furthermore, in contrast to methods such as co-precipitation or thermal decomposition, the sol-gel method offers a versatile framework for combining multiple metal precursors, facilitating the precise tuning of the structural and functional properties of the support material [33]. It also enables the creation of well-dispersed active sites, which are key to achieving superior catalytic efficiency in CO_2 methanation reactions [32]. Various sol-gel synthesis routes have been reported for preparing MA spinel supports, differing in precursor selection, complexing agents, and processing conditions. Some methods use water-based solutions with citric acid as a chelating agent, followed by direct gelation and calcination [34]. Others utilize organic solvents like diethylene glycol to improve the homogeneity of the precursor gel [27], while some incorporate carbon-based additives to modify the microstructure [35]. These methods generally require heating solutions to temperatures of 80–125 °C to form the desired viscous gel structure. In contrast, this study employed a simple, room-temperature sol-gel method.

In addition to these advantages, the sol-gel method is cost-effective and energy-efficient, particularly when compared to methods requiring high-temperature treatments (e.g., above 1000 °C) or the use of expensive organic solvents and additional carbon sources. The sol-gel process employed in this study operates at moderate temperatures without costly additives, reducing material and energy consumption while simplifying the synthesis procedure. This makes it a practical option for catalytic applications. Moreover, compared to solvent-based methods, this approach is more environmentally friendly and cost-effective, while still maintaining control over phase purity and surface properties. Thus, the sol-gel method's ability to provide precise structural control, high surface area, and economic feasibility makes it an ideal choice for developing efficient catalyst support materials in CO_2 methanation reactions. While the sol-gel method was chosen for support synthesis due to its structural and surface control, the wet impregnation method was selected for catalyst synthesis. This method ensures uniform distribution of metal precursors on the support, which is essential for achieving the desired catalytic properties [36, 37]. Although sol-gel processing could also be applied to catalyst preparation, wet impregnation was preferred in this study as it provides better control over metal dispersion and loading [38]. This technique has been widely used in the literature to synthesize highly active catalysts, particularly for CO_2 methanation reactions.

Thus, in this study, the MA support was synthesized via the sol-gel method, followed by the incorporation of Ni, NiFe and NiCo through a wet impregnation technique. The resulting catalysts were evaluated for their performance in CO_2 methanation reactions conducted at 350 °C and atmospheric pressure. This study aims to overcome key challenges in CO_2 methanation, offering a promising pathway

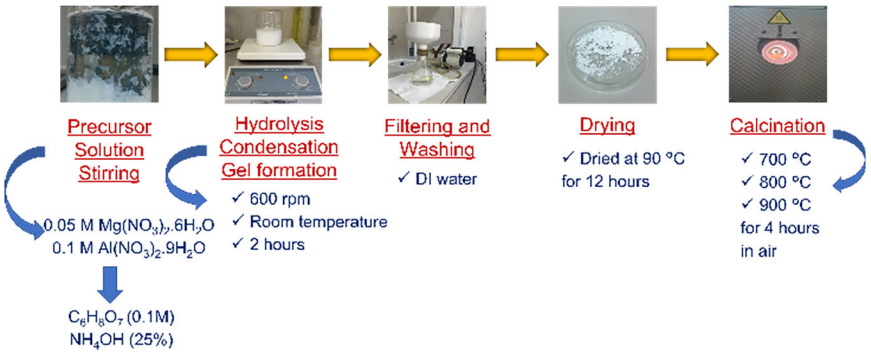

Fig. 1 Flowchart illustrating the sol-gel synthesis steps used for $MgAl_2O_4$ support materials preparation

for the development of efficient and cost-effective catalysts operating under low-temperature conditions. While various one-pot sol-gel approaches have been reported for synthesizing metal-doped spinel catalysts, such methods often suffer from limited control over metal dispersion and surface accessibility. In contrast, this study adopts a two-step strategy involving sol-gel derived support synthesis followed by wet impregnation of metal precursors, which enables better control over the distribution and interaction of active sites [38]. This approach not only simplifies the synthesis process but also provides improved structural stability and catalytic performance, as demonstrated in later sections. The benefits of this method are further emphasized through comparison with literature-reported one-pot sol-gel catalysts, which typically exhibit lower CO_2 conversion under similar reaction conditions [39–42].

Thermogravimetric analysis (TGA), X-ray diffraction (XRD), Fourier transform infrared spectroscopy (FT-IR), Brunauer-Emmett-Teller (BET) analysis, field emission scanning electron microscopy (FESEM), energy-dispersive X-ray spectroscopy (EDS), and transmission electron microscopy (TEM) were used to analyze the produced materials. The catalytic performance was initially tested using our high-throughput catalyst performance analysis system (HT-CPA) under atmospheric pressure. HT-CPA analysis results were used to identify the promising promoters. Subsequently, selected catalysts were further evaluated in our conventional catalytic performance analysis test system (C-CPA) to observe their performance under realistic reaction conditions. To understand catalytic mechanisms, catalysts were characterized by H_2 temperature programmed reduction (H_2-TPR) and CO_2 temperature-programmed desorption (CO_2-TPD) techniques.

2 Experimental

2.1 Supports synthesis

The experimental setup is illustrated in Fig. 1 The MA support material was synthesized using the sol-gel method (SG) from an aqueous solution 0.05 M $Mg(NO_3)_2{\cdot}6H_2O$ (99%, Sigma-Aldrich) and 0.1 M $Al(NO_3)_3{\cdot}9H_2O$ (98.5%, Sigma-Aldrich) with a molar ratio of Mg:Al = 1:2. A chelating agent, citric acid (0.1 M $C_6H_8O_7$), and a precipitating agent, NH_4OH (ACS reagent, 25% NH_3 basis), were added dropwise until precipitation began, maintaining the pH at around 10. The solution was continuously stirred for 2 h using a magnetic stirrer and allowed to age at room temperature overnight. The precipitates were filtered, washed with deionized water, and then dried overnight at 90 °C in an oven. This synthesis approach differs from conventional sol-gel methods in that it is carried out entirely at room temperature, using water as the solvent, without the need for heating during gelation or the use of organic solvents. The combination of citric acid as a chelating agent and pH adjustment with ammonia enhances precursor homogeneity and facilitates spinel formation at relatively low calcination temperatures. The dried samples were calcined at different temperatures (700, 800, 900 °C) in air for 4 h.

2.2 Catalysts synthesis

MA spinel powder was used as the support material to prepare three catalysts: Ni-MA, NiFe-MA, and NiCo-MA. The catalysts were synthesized using the wet impregnation method [34, 43], with Ni as the active metal and Fe or Co as promoters. The purpose of the promoters is to improve the dispersion of Ni active sites, the acid-base properties of the support, Ni-support interaction, and therefore the catalytic activity and stability of the catalyst. The MA support was impregnated with the aqueous solutions of $Ni(NO_3)_2{\cdot}6H_2O$ (99.99 + %, Sigma-Aldrich) and $Fe(NO_3)_3{\cdot}9H_2O$ (99 + %, Sigma-Aldrich) or $Co(NO_3)_2{\cdot}6H_2O$ (99 + %, Sigma-Aldrich). Ni was added to achieve a loading of 15 wt %. Subsequently, Co or Fe was added at a molar ratio of 2:1 relative to Ni. Each sample were sonicated for 2 h in an ultrasonic bath, dried overnight at 100 °C, and calcined at 600 °C for 3 h in air. Finally, the calcined catalysts were crushed and sieved to a particle size range of 50–100 µm to be used in the experiments.

2.3 Catalytic tests

2.3.1 High-throughput catalyst performance analysis

The CO_2 methanation performance of the prepared catalysts were initially evaluated using a high-throughput catalyst performance analyzer (HT-CPA). HT-CPA, described in detail elsewhere, is a computer-integrated high-throughput catalyst screening system that enables fast screening of multiple (max. 80) catalysts simultaneously [43, 44]. Reactant gases are mixed and fed to the system using calibrated mass flow controllers. The feed flow is distributed to four reactors each containing 20 microreactors. Each microreactor receives equally distributed gas flow and requires approximately 20 mg of catalyst. Outlet gases from the microreactors are sampled using a capillary sampling probe and sent directly to an online micro-Gas Chromatograph (micro-GC Fusion, Inficon), comprising RT-Q Bond and RT-Molecular Sieve 5 A models equipped with thermal conductivity detectors (TCD). Temperature, inlet flow rates, gas sampling, and movement of the reactor in the HT-CPA system are controlled via automated software.

Prior to the reaction, catalysts were reduced in-situ in the HT-CPA under a flow of 50% H_2 (Linde, 99.999%) / 50% N_2 (Linde, 99.999%) (v/v) mixture at 350 °C for 4 h. Following reduction, the CO_2 methanation reaction was initiated by feeding the reactant gas mixture composed of 64% H_2, 16% CO_2 (Linde, 99%), and 20% N_2 (v/v/v).

2.3.2 Conventional catalytic performance analysis

The prepared catalyst (0.5 g, particle size between 50 and 100 µm) was mixed with quartz (Sigma-Aldrich, purum p.a.) of the same particle size with a volumetric ratio of 1:1, and loaded into a fixed-bed reactor (10 mm i.d., 800 mm length). Prior to the reaction, the catalysts were activated at 350 °C for 2 h under a flow of 50 vol% H_2/50 vol% N_2, with a flow rate of 6 L/h·gcat. The reaction was performed at 350 °C and atmospheric pressure with a flow of 20 L/h·gcat using a 64 vol% H_2/16 vol% CO_2/20 vol% N_2 mixture. Gas analysis was performed using an online gas chromatograph (Agilent, GC 7820) equipped with a TCD and a flame ionization detector (FID), with Carboxen and Alumina S columns, respectively.

CO_2 conversion, product selectivity and carbon based methane yield were calculated by the following equations:

$$X_{CO_2} = \frac{F_{CO_{2,in}} - F_{CO_{2,out}}}{F_{CO_{2,in}}} \times 100 \quad (4)$$

where X_{CO_2} is the percent CO_2 conversion, $F_{CO_{2,in}}$ is the molar flow rate of CO_2 at the inlet (mol/h) and $F_{CO_{2,out}}$ is the molar flow rate of CO_2 at the outlet (mol/h). The selectivity and yield of the products are calculated using the following equations below:

$$S_{CO} = \left(\frac{nc_{CO} \times F_{CO_{out}}}{F_{CO_{2,in}} - F_{CO_{2,out}}}\right) \times 100 \quad (5)$$

$$S_{CH_4} = \left(\frac{nc_{CH_4} \times F_{CH_{4,out}}}{F_{CO_{2,in}} - F_{CO_{2,out}}}\right) \times 100 \quad (6)$$

$$S_{C_2H_6} = \left(\frac{nc_{C_2H_6} \times F_{C_2H_{6,out}}}{F_{CO_{2,in}} - F_{CO_{2,out}}}\right) \times 100 \quad (7)$$

$$\%Y_{CH_4} = \left(\frac{F_{CH_{4,out}}}{F_{CO_{2,in}}}\right) \times 100 \quad (8)$$

where S represents the carbon based product selectivity, Y represents the percent yield of the products, nc is the carbon number of the specified product, and $F_{CO_{out}}$, $F_{CH_{4,out}}$, and $F_{C_2H_{6,out}}$ denote the outlet molar flow rates (mol/h) of CO, CH_4 and C_2H_6, respectively. Selectivity of methane regarding only gas products can be calculated with the following equation:

$$S_{CH_4 in\ gas} = \left(\frac{F_{CH_{4,out}}}{F_{CH_{4,out}} + F_{CO_{out}} + F_{C_2H_{6,out}}}\right) \times 100 \quad (9)$$

Methane yield on a carbon basis is calculated with the following equation:

$$Y_{CH_4} = \frac{nc_{CH_4} \times F_{CH_{4,out}} \times MW_C}{M_{active\ metal} \times 3600} \left(\frac{g\ CH_4\ on\ C\ basis}{g\ active\ metal \times s}\right) \quad (10)$$

where Y_{CH_4} represents the carbon based methane yield in units given in the parenthesis, MW_C is the molecular weight of carbon in grams, and $M_{active\ metal}$ is the weight of the active site in grams, and 3600 is for the unit conversion from hour to seconds.

2.4 Characterization

Thermochemical simulations were performed using the Phase Diagram and Equilib modules of FactSage™ 8.2 to predict the possible phases in supports and catalysts [45]. Thermogravimetric analysis (TGA) and derivative thermogravimetry (DTG) were carried out using a TGA 55 model (TA Instruments) to investigate the thermal decomposition behavior of the nanoparticles. The measurements were performed on the dried nanoparticles over a temperature range of 10–900 °C, at a heating rate of 10 °C/min, in an air atmosphere. Fourier transform infrared spectroscopy (FTIR) (Bruker Alpha-II) was measured in the range of 4000–400 cm^{-1} in order to understand the chemical

bonding of the nanoparticles. X-ray diffraction patterns of the samples were obtained using a Philips PAN'alytical X'Pert Pro model instrument over a 2theta (2θ) diffraction angles range of 10–90° at 1°/min scanning speed using monochromatic Cu Kα radiation (λ = 1.5418 Å, 40 mA, 45 kV). Brunauer-Emmett-Teller analysis (BET) (Micromeritics, Tristar3000) based on N_2-adsorption at 77 K was performed to obtain the specific surface areas of the supports and catalysts. Before taking adsorption isotherms, all samples were degassed at 250 °C for minimum 6 h. The pore volume and average pore size distribution were calculated by the Barret-Joyner-Hallender (BJH) method using the N_2 adsorption isotherm. The morphology of the nanoparticles was characterized using a HITACHI SU5000 model scanning electron microscope (SEM). For the SEM analysis, nanoparticles placed on carbon tape were coated with gold inside a Quorum/Polaron SC7620 high-resolution sputter coater. To image inside the nanoparticles, transmission electron microscopy (TEM) was used. For these experiments, the nanoparticles were dispersed in ethanol. The resulting solutions were transferred onto carbon-coated Cu TEM grids and allowed to dry. TEM images were obtained at various magnifications with an accelerating voltage of 200 kV using a FEI TALOS F200S. Selected Area Electron Diffraction (SAED) and Energy Dispersive X-ray Spectroscopy (EDS) techniques were also applied to analyze the crystalline structure and elemental composition of the nanoparticles.

The reducibility behavior of catalysts were determined by H_2-temperature programmed reduction (H_2-TPR) in a fixed bed reactor. The reduction step is essential to ensure that the catalyst is in its active metallic state, as certain metal oxides, such as those containing Ni or Co, must be reduced to their metallic form for optimal activity in reactions like CO_2 methanation. The reduction process helps remove surface oxygen species and activates the metal sites, making them available for interaction with reactants. In TPR measurements, first, 0.15 g of catalyst was preheated in a N_2 flow at 350 °C for 30 min. Then, the reactor temperature was first decreased to 50 °C and then increased to 700 °C at a rate of 10 °C min^{-1} under a 80 mL·min^{-1} gas mixture of 10 v% H_2 in balance N_2. Data were collected by both an on-line micro GC equipped with a TCD and an on-line mass spectrometer (MS) (Stanford Research Systems, RGA 200). The surface basicity of the samples was determined by the temperature programmed desorption of CO_2 (CO_2-TPD) (Quanta Chrome, CHEMBET-3000) in the same system used for H_2-TPR analyses. CO_2-TPD is employed to assess the distribution and strength of the basic sites on the catalyst surface, which play a crucial role in CO_2 adsorption and activation during methanation. In CO_2-TPD analyses, 0.15 mg catalyst was thermally treated and reduced under 53 mL min^{-1} H_2 flow for 2 h at 350 °C. Then catalysts were purged with a 100 mL min^{-1} N_2 for 30 min at 350 °C. Afterward, the temperature was reduced to 50 °C. The CO_2 adsorption was conducted with a 100 mL min^{-1} gas mixture of 10% CO_2 and 90% N_2 at 50 °C for 30 min. Then physisorbed CO_2 was swept away by a 100 mL min^{-1} N_2 for 30 min. In the desorption step of chemisorbed CO_2, the temperature was increased from 50 to 700 °C with a ramp of 10 °C min^{-1} under 100 mL min^{-1} N_2 flow. The CO_2 desorption profiles were obtained through detecting the desorbed amount of CO_2 at the corresponding desorption temperature by a micro GC and a MS.

3 Results and discussion

3.1 Thermochemical modeling

Thermochemical calculations were performed using the FactSage™ software by selecting the FactPS (pure substances) and FToxid (oxide solutions) databases to predict the phase changes and phase diagrams of the catalyst system under various composition and calcination conditions. Figure 2 shows the thermochemical modeling results for the effect of Co substitution for Fe on the phase changes in a system made up of 100 parts by mass $MgAl_2O_4$, 15 parts Ni, and 30 parts Fe, at 600 °C, under a total pressure of 1 atm and an oxygen partial pressure of 0.21 atm. The results indicate that a high Fe content increases the formation of the spinel phase. With 15 parts Fe, the spinel structure becomes saturated, leading to the formation of a small amount of corundum (1.3 wt.% Fe_2O_3). As Co gradually replaces Fe, the corundum phase disappears first, and then a monoxide phase begins to form at the expense of the spinel phase. When Fe is completely replaced by Co (30 parts Co), the total amount of the monoxide phase remains low, around 6.65 wt.%. This phase mainly consists of NiO (52.31 wt.%) and MgO (45.15 wt.%), with a small amount of CoO (2.54 wt.%).

Figure 3 presents the phase diagrams obtained from thermochemical modeling, illustrating the phase evolution as a function of calcination temperature and oxygen partial pressure for two systems: (a) 100 parts by mass $MgAl_2O_4$ with 15 parts Ni, and (b) 100 parts by mass $MgAl_2O_4$ with 15 parts Ni and 30 parts Co. In both systems, the spinel and monoxide phases dominate over a wide temperature range and at relatively high oxygen partial pressures. Under the experimental conditions of 600 °C and an oxygen partial pressure of 0.21 atm, the calculated phase fractions for the Ni-containing system (Fig. 3a) were 88 wt% spinel and 12 wt% monoxide. In the system containing both Co and Ni (Fig. 3b), a slight increase in the spinel phase to 93.35 wt% and a corresponding decrease in the monoxide phase to 6.65 wt% were observed.

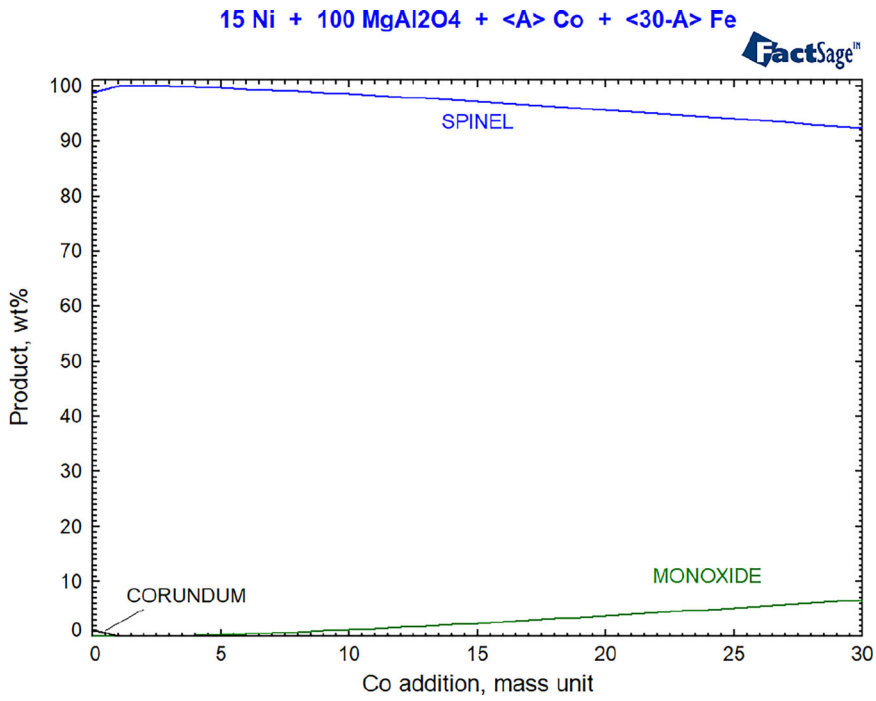

Fig. 2 Thermochemical modeling of the effect of Co substitution for Fe on phase evolution in Ni-Fe-Co-O-$MgAl_2O_4$ system at 600 °C under $pO_2 = 0.21$ atm

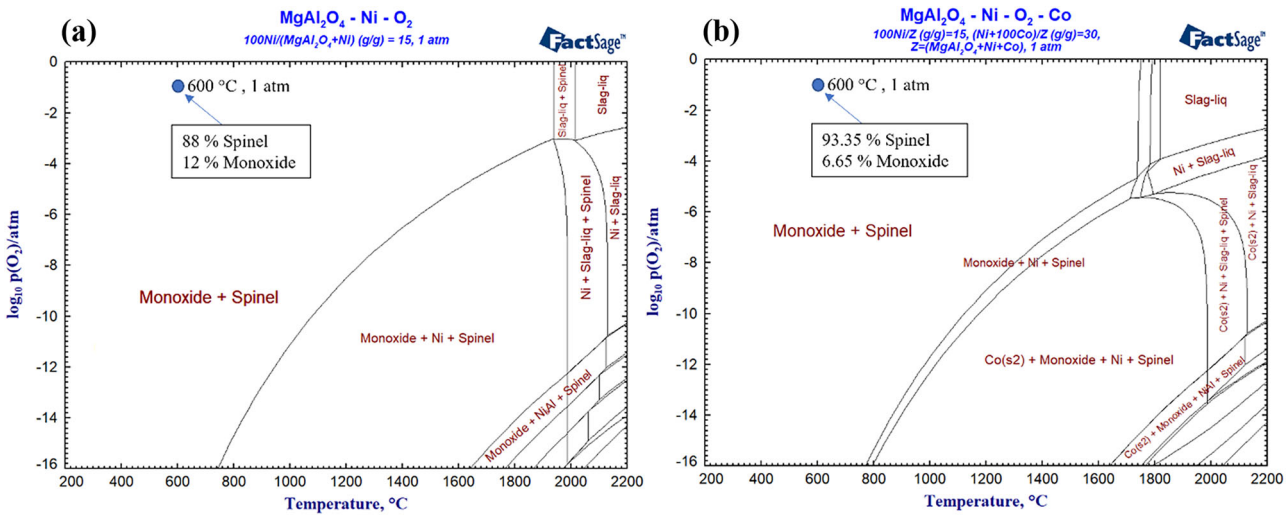

Fig. 3 Calculated phase diagram for (**a**) Ni-O-$MgAl_2O_4$ and **b** Co-Ni-O-$MgAl_2O_4$ systems as a function of calcination temperature and oxygen partial pressure

For catalytic applications, the stabilization of the spinel structure is crucial, as it enhances metal dispersion and thermal stability. While moderate amounts of the monoxide phases (e.g., NiO, CoO, and MgO) may facilitate CO_2 activation and improve metal dispersion, their excessive formation can lead to phase segregation, reduce the number of accessible active sites, and ultimately impair catalytic performance. Therefore, maintaining spinel structure with limited oxide phases is considered beneficial for ensuring optimal catalytic performance [24, 40, 46].

3.2 TG-DTG analysis

The TGA-DTG curves of the uncalcined MA powder are presented in (Online Resource Fig. S1). These complementary analyses provide a comprehensive understanding of the thermal behavior and stability of the material. While the TGA curve (red) displays the total weight loss, the DTG curve (blue) provides the rate of decomposition, highlighting the stages of degradation and stabilization. The TGA curve indicates that weight loss occurs in multiple stages. An initial weight loss between

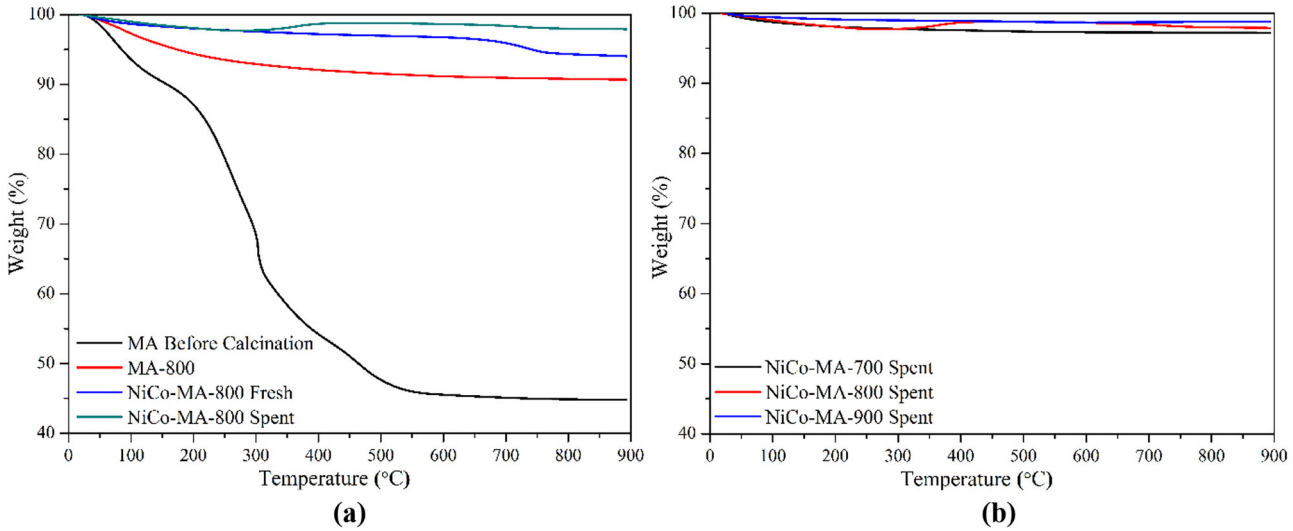

Fig. 4 TGA analysis of (**a**) uncalcined MA, MA-800, and NiCo-MA-800 fresh and spent catalysts, **b** spent NiCo-MA catalysts under air atmosphere

100 and 200 °C is attributed to the removal of adsorbed water and decomposition of volatile organic components. A more significant weight loss is observed between ~200 and 400 °C, which corresponds to dehydration processes and the removal of residual organics, contributing to the formation of oxide species. No notable weight change is observed above 600 °C, suggesting the complete removal of volatiles and thermal stabilization of the material. However, the crystallization and phase transformation toward a spinel structure likely continue at higher temperatures [47].

The DTG curve reveals that the rate of weight loss is highest between 200 and 400 °C, corresponding to the dehydration and decomposition stages. A sharp peak at around 300 °C corresponds to rapid weight loss due to the decomposition of organic molecules. A peak around 450 °C likely corresponds to structural reorganization and early-stage crystallization of intermediate oxide species. The gradual decline in the weight loss rate confirms that the main thermal decomposition processes are complete, and minimal change above 600 °C further supports the thermal stabilization of the material.

In addition to the uncalcined MA support, TGA analyses were performed on the MA-800 and NiCo-MA-800 catalysts, both before and after reaction (Fig. 4a). In the TGA of calcined MA, no significant weight loss was observed. This was reasonable since calcination has already led to the removal of water, nitrates, and organics species before TGA measurement, as well as the initial formation of metal oxide phases that has been discussed above. The NiCo-MA-800 fresh catalyst also showed minimal weight loss (<3%), confirming the thermal stability of the metal-incorporated spinel support. Interestingly, both fresh and spent catalysts exhibited a slight weight gain between 300 and 500 °C, likely due to the surface oxidation of metallic Ni and/or Co species. This is followed by a small weight loss up to 600 °C due to the oxidation of residual carbonaceous species. These results highlight the thermal durability of the catalyst and its suitability for high-temperature CO_2 methanation [48].

To further assess coke formation and possible surface oxidation during reaction, TGA analyses were also performed on the spent NiCo-MA catalysts (Fig. 4b). All samples exhibited very low total weight losses (~1.2–2.8%), indicating limited or no carbon deposition throughout the methanation process consistent with enhanced coke resistance. Studies have demonstrated that incorporating Co in Ni catalysts supported on MA can enhance coke resistance as reported by Aramouni et al. Suppressed coking was claimed to be inherently due to the high oxygen affinity of Co contributing to C* oxidation (oxidative removal of adsorbed carbon atoms from the catalyst surface) [49]. However, although a higher resistance to coking was observed in Ni-Co bimetallic catalysts, carbon formation was unlikely to be completely avoided. Therefore, a better understanding of coke formation even in trace amount is needed to prevent the gradual catalytic deactivation. Even in trace quantities, most carbon has been seen to be removed below 600 °C in TGA plots, indicating that amorphous carbon typically forms rather than graphitic carbon [50]. Amorphous carbon is known to be thermally less stable, which is advantageous in terms of catalyst regeneration at mild temperatures below 550 °C.

3.3 Fast screening of catalysts using HT-CPA

The nine catalysts prepared by impregnating Ni, NiFe or NiCo onto MA supports calcined at 700 °C, 800 °C and

Table 1 CO_2 methanation performance of catalysts in HT-CPA

No	Calcination Temperature (°C)	Sample	CO_2 conversion %	CH_4 Yield %	CH_4% (GC)
1	700	Ni-MA	15.70	12.98	2.60
2		NiFe-MA	11.10	13.67	2.56
3		NiCo-MA	52.80	52.88	12.45
4	800	Ni-MA	33.06	31.96	6.98
5		NiFe-MA	48.93	41.51	9.92
6		NiCo-MA	48.66	45.82	10.72
7	900	Ni-MA	46.82	30.45	7.79
8		NiFe-MA	31.77	25.34	6.30
9		NiCo-MA	73.02	40.12	15.78

900 °C were initially screened for their catalytic performance using HT-CPA, as described earlier. This step was performed to identify the highest-performing catalysts to perform a more detailed performance analysis in the conventional test system. The results for CO_2 conversion, CH_4 yield and CH_4 selectivity are summarized in Table 1. Based on these results, the NiCo-MA catalysts were selected for further analysis due to their high CO_2 conversion, CH_4 yield and selectivity compared to the others, making them the most promising candidates for detailed evaluation using the conventional test system.

The observed catalytic performance is partially explained by the thermodynamic insights presented in Section "Thermochemical Modeling". The NiCo-MA catalysts exhibited the highest CO_2 conversion and CH_4 yield at all calcination temperatures, consistent with the thermochemical equilibrium calculations. At 900 °C, their performance significantly improved (CO_2 conversion: 73.02%, CH_4 yield: 40.12%, CH_4 selectivity: 15.78%). This can be attributed to the favorable stabilization of the spinel phase, which predominated at higher calcination temperatures. This stabilization enhanced metal dispersion and thermal stability while reducing the formation of undesirable phases, such as the monoxide phase. However, at all calcination temperatures, the Ni-MA and NiFe-MA catalysts showed lower CO_2 conversion and CH_4 yield. At 800 °C, the NiFe-MA catalysts showed slight improvement, but their performance was still lower compared to the NiCo-MA catalysts. This may be due to the poorer spinel stability in Ni-MA catalysts and the development of less stable phases in NiFe-MA catalysts. Given their strong CO_2 conversion and CH_4 selectivity, the NiCo-MA catalysts are suitable for further investigation in the conventional test system. Our results confirm that the NiCo-MA catalysts are the most attractive candidates for a thorough performance evaluation. The experimental findings are in good agreement with the phase stability predictions in Section "Thermochemical Modeling", especially the dominance of the spinel phase, highlighting the importance of phase stability in maximizing catalytic performance.

3.4 FT-IR analysis

The FT-IR spectra of sol-gel-derived MA particles before calcination and after calcination at 700, 800, and 900 °C are presented in Fig. 5a. The uncalcined sol-gel-derived sample (MA-SG) exhibited functional groups, such as −OH [51], and typically an amorphous structure [52]. During calcination, these functional groups undergo decomposition, forming M − O − M bonds as the amorphous structure transitions to a crystalline spinel phase.

The FT-IR spectrum of MA-SG revealed a broad band at 3000–3600 cm^{-1} and a peak at 1650 cm^{-1}, corresponding to the stretching and bending vibrations of −OH groups, respectively, of water [53, 54]. The band at ~1315 cm^{-1} was attributed to N − O bond vibrations from nitrate $(NO_3)^-$ groups [54], and weak bands at ~1040 cm^{-1} were assigned to Al−O − H bonds [55]. Peaks in the 800–500 cm^{-1} range were associated to Al−O [56] and Mg−O [57] vibrations.

Calcination significantly reduced the intensity of the peaks associated with functional groups. After calcination at 700 °C, a broad peak at 3000–3600 cm^{-1} and vibrations of −OH groups around 1650 cm^{-1} were still present. These peaks diminished significantly at 800 °C and disappeared entirely at 900 °C. The absorbance bands at 670–678 cm^{-1} and 469–474 cm^{-1} confirmed the presence of AlO_6 groups, confirming the formation of MA spinel at all calcination temperatures [53–58]. The increasing calcination temperature enhanced the intensity of the Al−O−Mg bond vibrations, indicating the progression of crystallization [27]. The absence of nitrate or organic group bands in the calcined samples demonstrates the high surface purity and complete formation of the spinel structure [30].

Figure 5b presents the FT-IR spectra of MA calcined at 800 °C, both before (fresh) and after (spent) being used in the reaction. The spectra confirmed the presence of characteristic vibrations of the spinel structure, with bands in the 500–900 cm^{-1} region corresponding to the stretching vibrations of aluminum–oxygen (Al–O), metal–oxygen (M–O), and metal–oxygen–aluminum (M–O–Al) bonds [59, 60]. In the fresh catalyst, Al−O−Mg and AlO_6 vibrations were observed. However, a noticeable reduction in the relative intensity of these peaks was observed in the spent catalyst, attributed to the formation of coke deposits on the catalyst surface [15, 61]. For investigating coke formation on catalysts, the FT-IR technique provides a useful method. A distinct marker of coke deposition is the elimination or significant reduction of specific vibrational bands present in the fresh catalyst. Since the spent catalyst lacks these bands, which are connected to specific functional groups or surface contacts, it is possible that the buildup of carbonaceous residues has

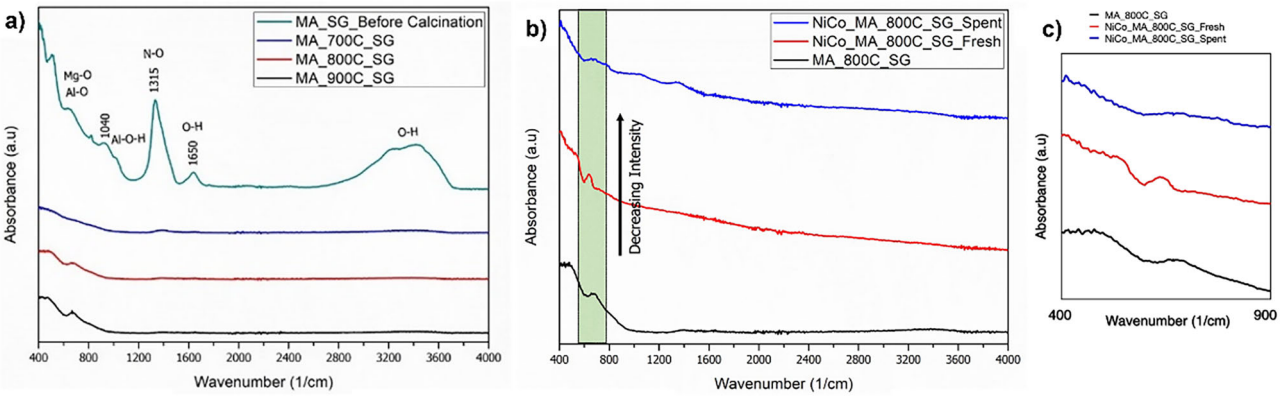

Fig. 5 FT-IR spectra of MA powders prepared by the SG method: (**a**) The green curve represents the sample before calcination, while the blue, red, and black curves correspond to the samples calcined at 700 °C, 800 °C, and 900 °C for 4 h, respectively, **b** calcined at 800 °C: support (black curve), fresh catalyst (red curve) and spent catalyst (blue curve), **c** coomed in view of the 400–900 cm^{-1} region

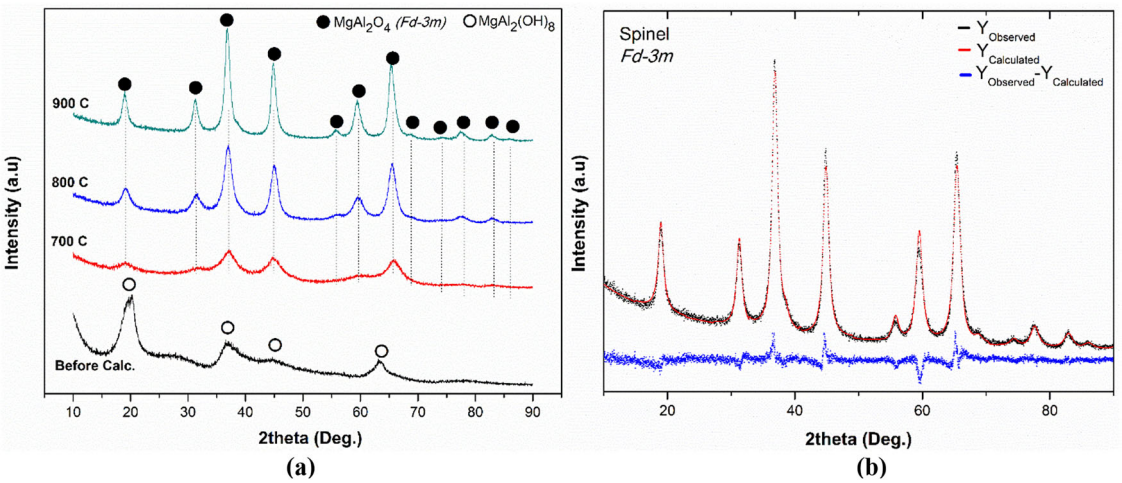

Fig. 6 **a** XRD patterns of $MgAl_2O_4$ powders prepared by the SG method before (black) and after calcination at 700 °C (red), 800 °C (blue), and 900 °C (green) for 4 h. **b** The Rietveld analysis result of the MA spinel ($R_{exp} = 5.22$, $R_p = 5.70$, $R_{wp} = 7.28$, GoF = 1.94)

altered or blocked these active sites entirely (Fig. 5c). The formation of coke layers prevents infrared beam penetration, leading to decreased signal transmission [61, 62]. Coke formation, which occurs primarily on metal oxide sites (e.g., Al–O or M–O), can lead to the development of surface carbon layers. These sites provide adsorption centers for CO_2 and H_2, leading to the formation of carbonaceous intermediates. Oxygen vacancies and electron transfer processes on metal oxides further facilitate the stabilization of these intermediates, which can subsequently polymerize and accumulate as coke deposits [63]. Over time, these deposits develop into carbon layers that not only reduce the intensity of the characteristic vibrational bands but also block active sites, ultimately diminishing the catalyst's performance in CO_2 methanation.

3.5 XRD analysis

As shown in Fig. 6a, the typical diffraction peaks of $MgAl_2O_4$ spinel (ICDD: 01-075-1796) were observed in the sample after heating at 700 °C, indicating the formation of $MgAl_2O_4$ at this temperature. In contrast, the as-synthesized powders were predominantly composed of $MgAl_2(OH)_8$, likely highly defective and nanocrystalline, with a structure close to amorphous. The intensity of the $MgAl_2O_4$ diffraction peaks increased as the temperature was raised from 700 to 900 °C. At higher temperatures, even the lowest-intensity peaks corresponding to the *Fd-3m* crystal structure became visible, indicating improved crystallinity.

From the XRD data in Fig. 6, the crystallite sizes of $MgAl_2O_4$ were calculated using the Debye-Scherrer equation (Eq. 11),

$$D = \frac{K \times \lambda}{\beta \times \cos\theta} \tag{11}$$

where K is the Scherrer constant (typically 0.9 for spherical particles), λ is wave-length of the X-ray beam used (1.5418 Å), β is the full width at half maximum (FWHM) of the peak and θ is the Bragg angle [64–66]. This equation

accounts only for peak broadening due to crystallite size. Since peak broadening is inversely proportional to crystallite size, smaller crystallites yield broader diffraction peaks. Given that $MgAl_2O_4$ was synthesized as a nanosized material, its diffraction peaks appeared broad and of low intensity, indicating a fine crystallite size. The crystallite sizes were calculated for different diffraction planes ((220), (311), (400), (511), and (440)) using the Scherrer equation. The final crystallite size for each sample was obtained by averaging these values, as presented in Table 2. As the calcination temperature increased (700–900 °C), the crystallite size also increased, reflecting enhanced crystallinity.

Rietveld analysis revealed that the refined unit cell of $MgAl_2O_4$ adopts the cubic *Fd-3m* space group, with a lattice parameter of 8.0546 Å. Notably, no significant peaks corresponding to possible intermediate products, such as Al_2O_3 or MgO, were detected, indicating that the final product consisted solely of $MgAl_2O_4$ crystals (Fig. 6b). According to the phase diagram simulations by FactSage™, even if more Al_2O_3 appears in the phase diagram (i.e., less Mg), a spinel solution region can still form, and the structure will contain only Mg vacancies. The atomic positions and lattice parameters derived from the Rietveld analysis confirm that less Mg is present than theoretically expected, but the crystal structure remains that of $MgAl_2O_4$ spinel.

Table 2 Crystallite size of $MgAl_2O_4$ spinel calculated from XRD patterns using the Debye–Scherrer equation

Sample	Crystallite size (nm)					Average crystallite size (nm)
	(220)	(311)	(400)	(511)	(440)	
MA700	2	2	3	2	3	2
MA800	4	5	6	4	6	5
MA900	8	8	9	7	8	8

The XRD analysis of the catalysts prepared via the wet impregnation method revealed that the fresh catalysts exhibit peaks corresponding to the spinel structure and NiO. A more detailed examination, supported by Rietveld analysis, identified two distinct spinel phases: Spinel-1 (Mg-Al rich) and Spinel-2 (Co rich, likely Co_3O_4 or $CoAl_2O_4$) both adopting the *Fd-3m* space group (Fig. 7) [12]. It was observed that the Spinel-1 peaks were broadened and of somewhat lower intensity compared to Spinel-2. Additionally, lattice strain and structural distortions within the $MgAl_2O_4$ framework may further contribute to peak broadening. The presence of such distortions is supported by the observed increase in the Rietveld-fitted lattice parameters for the $MgAl_2O_4$ phase to 8.10 Å, 8.10 Å, and 8.073 Å for the 700 °C, 800 °C, and 900 °C calcined impregnated samples, respectively, compared to 8.0546 Å for the calcined unimpregnated substrates. This suggests that some Co and Ni could be incorporated into the $MgAl_2O_4$ spinel structure, leading to slight structural modifications. In contrast, Co_3O_4 exhibited sharper diffraction peaks, which is indicative of its relatively larger crystallite size. The lattice parameters for Co_3O_4 were 8.117 Å, 8.121 Å, and 8.115 Å, at 700 °C, 800 °C, and 900 °C, respectively, showing minimal variation. Similarly, the cubic NiO phase with the *Fm-3m* space group was confirmed through excellent Rietveld fitting (GoF values ranging from 1 to 1.5) and remained relatively constant at 4.181 Å, 4.182 Å, and 4.182 Å across the different calcination temperatures. The semi-quantitative Rietveld

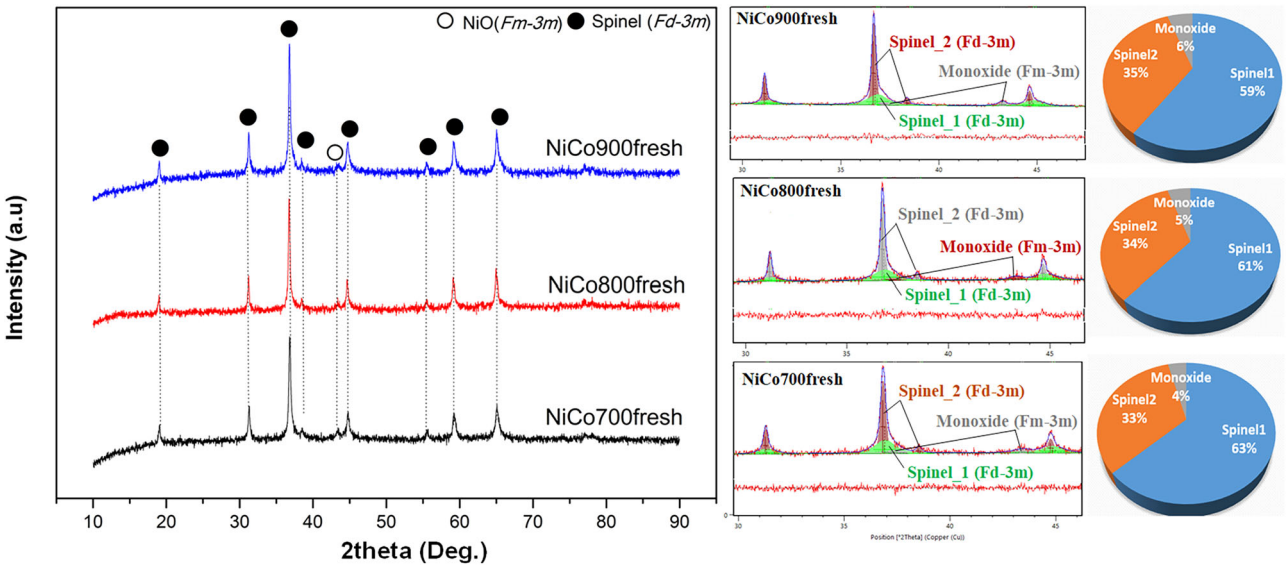

Fig. 7 XRD analysis results of NiCo-MA catalysts calcined at different temperatures and Rietveld fit results and peak deconvolutions for the fresh catalysts

analysis provided the relative phase compositions (in wt.%): 63 wt.% Spinel-1, 33 wt.% Spinel-2, and 4 wt.% Monoxide (Ni rich) for the NiCo700fresh sample; 61 wt.% Spinel-1, 34 wt.% Spinel-2, and 5 wt.% Monoxide (Ni rich) for the NiCo800fresh sample; and 59 wt.% Spinel-1, 35 wt.% Spinel-2, and 6 wt.% Monoxide (Ni rich) for the NiCo900fresh sample. These values remained relatively consistent within the margin of error.

In the spent catalyst, very faint peaks corresponding to spinel and NiO were observed (Online Resource Fig. S2). However, the strong suppression of spinel peaks by the SiO_2 signals introduced significant limitations in clearly distinguishing Co_3O_4, $MgAl_2O_4$, and even NiO, making quantitative phase analysis impossible. Despite these limitations, the scattered XRD peak profiles of the catalysts after usage appeared relatively similar. Furthermore, peaks corresponding to SiO_2 were identified, attributable to the 1:1 volumetric ratio of quartz used during catalyst preparation. It is important to note that XRD is typically used for detecting crystalline phases, while coke is usually an amorphous carbon material. Graphite formation, which requires higher temperatures (around 500 °C or higher) and conditions favoring its graphitization, is not expected under our reaction conditions (350 °C). Amorphous structures do not produce distinct diffraction peaks in XRD patterns, which is likely the reason why carbon or graphite peaks were not detected in the analysis. Moreover, the XRD technique has limited sensitivity to low-crystallinity compounds, which further complicates the detection of coke. In the case of our catalyst, the SiO_2 peaks were dominant, masking the visibility of other phases, including coke, in the diffraction pattern. Therefore, while coke formation was not detectable by XRD, the presence of carbon was confirmed through EDS analysis in the spent catalyst, supporting the formation of coke.

3.6 BET analysis

The N_2 physisorption results of the samples align with the type IV isotherm curve and the type H2 hysteresis loop in the IUPAC classification of adsorption isotherm with hysteresis loops, indicating the MA samples exhibit a mesoporous structure across all calcination temperatures. Additionally, pore widths derived from the BJH method are observable for the samples. As illustrated in Table 3, the average pore widths of the samples are mostly within the 2–10 nm range. This observation underscores that the supports prepared using the SG method exhibit characteristics consistent with typical mesoporous materials.

As summarized in Table 3, MA support materials were prepared at three different calcination temperatures: 700, 800, and 900 °C. The structural properties of these supports exhibited clear trends with increasing calcination temperatures. Specifically, higher calcination temperatures led to a decrease in surface area and pore volume, accompanied by an increase in average pore width, which reflects sintering and densification effects. Subsequently, Ni and Co were impregnated onto these supports via the wet impregnation method to synthesize the corresponding catalysts. After impregnation, significant reductions in surface area and pore volume were observed for all catalysts compared to their respective supports. For instance, the MA support calcined at 700 °C (MA700) exhibited a pore volume of 0.35 cm³/g, which decreased to 0.21 cm³/g for the NiCo-MA catalyst prepared from the same support. Similarly, the surface area decreased from 188 m²/g to 88 m²/g. A similar trend was observed for the catalysts prepared using supports calcined at 800 °C and 900 °C. The reduction in pore volume and surface area can be attributed to the incorporation of Ni and Co into the pore structure of the supports, which effectively blocks the pores and contributes to densification during calcination. These results indicate that both the initial calcination temperature of the support and the subsequent incorporation of active metals significantly influence the final structural properties of the catalysts.

Table 3 Structural properties of the support samples and the corresponding catalysts

Samples	BET surface area (m^2/g)	Average pore width (nm)	Specific pore volume (cm^3/g)
MA700	188	5.2	0.35
MA800	162	4.9	0.22
MA900	95	7.8	0.25
NiCo-MA700-Fresh	88	6.8	0.21
NiCo-MA800-Fresh	75	4.3	0.11
NiCo-MA900-Fresh	43	7.8	0.11

3.7 FESEM-EDS analysis

Figure 8 shows the FESEM images obtained at 100k magnification of the MA samples subjected to different calcination temperatures. The MA particles exhibit a nearly spherical morphology at the nanoscale, although smaller particles show signs of agglomeration. As the calcination temperature increased, both the particle size and the degree of agglomeration were observed to increase.

In Fig. 9, the FESEM results of the NiCo-MA catalyst, in which MA calcined at 800 °C was used as the support material, are shown. Upon examining the images of both the fresh and spent catalysts, an increase in agglomeration is evident, and a surface-covering structure is further observed, confirming the occurrence of coking.

EDS analysis was used to confirm the different elements in the MA, fresh and spent catalyst (Online Resource Fig. S3). The results show that the atomic percentage of magnesium in the support sample is 8.4 at % Mg, significantly

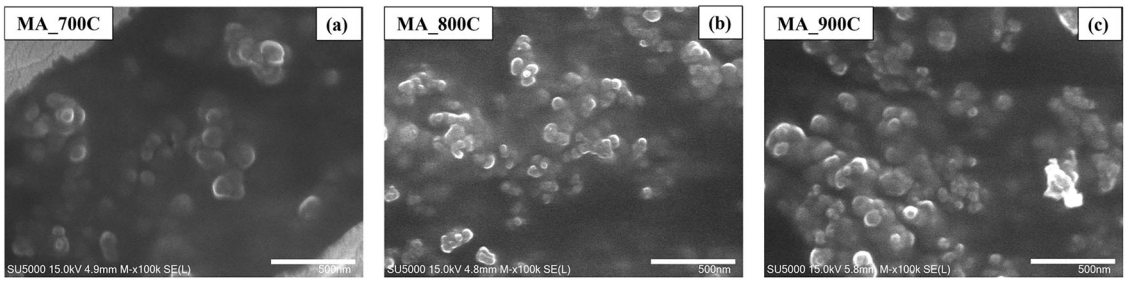

Fig. 8 FE-SEM images of MA supports calcined at different temperatures (**a**) 700 °C, **b** 800 °C, and **c** 900 °C

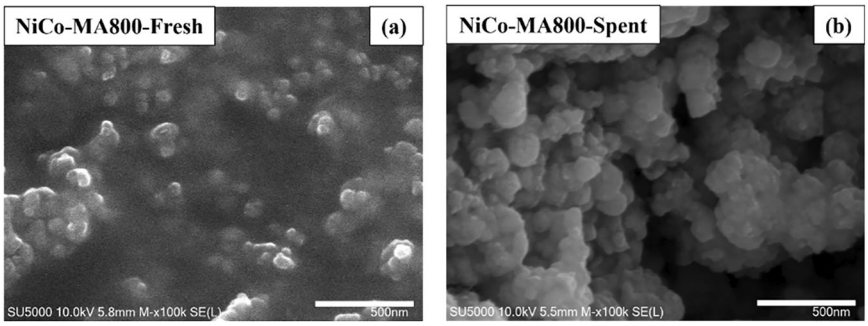

Fig. 9 FE-SEM images of NiCo-MA catalyst in which MA calcined at 800 °C **a** fresh catalyst **b** spent catalyst

lower than the expected 14.3 at % Mg. This indicates that the targeted Mg:Al molar ratio of 1:2 was not achieved. Furthermore, the analysis of both fresh and spent catalysts reveals clear carbon accumulation on the surface of the spent catalyst, confirming coking. This carbon build-up obscures the accurate determination of the metal element ratios.

3.8 TEM analysis

Figure 10a shows the TEM bright-field images of the MA support powders as calcined at 800 °C. The powders were found to be nanoscale, consisting of small, randomly oriented crystallites, which lead to a ring pattern indexed as the (311), (400), and (440) planes of Fd-3m spinel crystallites. The TEM images confirm the broadened XRD peaks and SEM observations. In contrast, the as-impregnated powders exhibited larger agglomerates (Fig. 10b). A detailed image (Fig. 10b) shows smaller crystallites alongside larger ones. Since the crystal structures and lattice plane distances of $MgAl_2O_4$, Co_3O_4, and $CoAl_2O_4$ spinels are similar, it is difficult to distinguish them solely based on the ring patterns. Furthermore, some lattice plane distances of the Fm-3m NiO phase, such as (111)Fm-3m/(311)Fd-3m and (200)Fm-3m/(400)Fd-3m, are very close to each other. This makes it challenging to focus on a single crystallite in SAED patterns due to the small crystallite sizes. Nevertheless, the SAED pattern and HRTEM lattice images demonstrated the (111) plane vectors of the spinel phase, superimposed with faint ring patterns, which correspond to the spinel peaks. HRTEM simulations confirmed that the observed planes are (111) planes of the Fd-3m space group, with a zone axis of [01-1]. Coupled with the XRD analysis, the small, randomly oriented crystallites can be attributed to the MA support, while the larger crystallites likely correspond to a Co-rich spinel phase. Since NiO is present in the smallest amount, as indicated by the Rietveld method, it was not distinctly observed in the SAED pattern. However, many randomly distributed diffraction spots are visible, and identifying the true NiO spots is difficult due to the good correspondence between the lattice planes of NiO and the spinel phases. The TEM-EDS mapping results (Online Resource Fig. S4) show that Co and Ni signals were prominent in the surface regions of the particles, as demonstrated in the mixed mapping image. In contrast, Mg and Al signals were very faint. Additionally, Ni and Co segregation was observed in these particles, at least within the resolution limits of the EDS detector.

In Fig. 11, the TEM analysis of the spent catalyst, crystalline phases was observed together with the presence of amorphous content. Upon closer examination, crystalline planes were discernible; however, globular content lacking a planar arrangement was also evident. This suggests that coking may be pronounced in this sample, supported by the XRD patterns indicating the crystalline nature of SiO_2. The presence of crystalline SiO_2 could reduce surface area and hinder metal dispersion, thereby facilitating coke formation. Furthermore, the SAED patterns revealed that the (101) spots of the SiO_2 phase are superimposed on the generic spinel ring pattern, supporting the idea that SiO_2 may

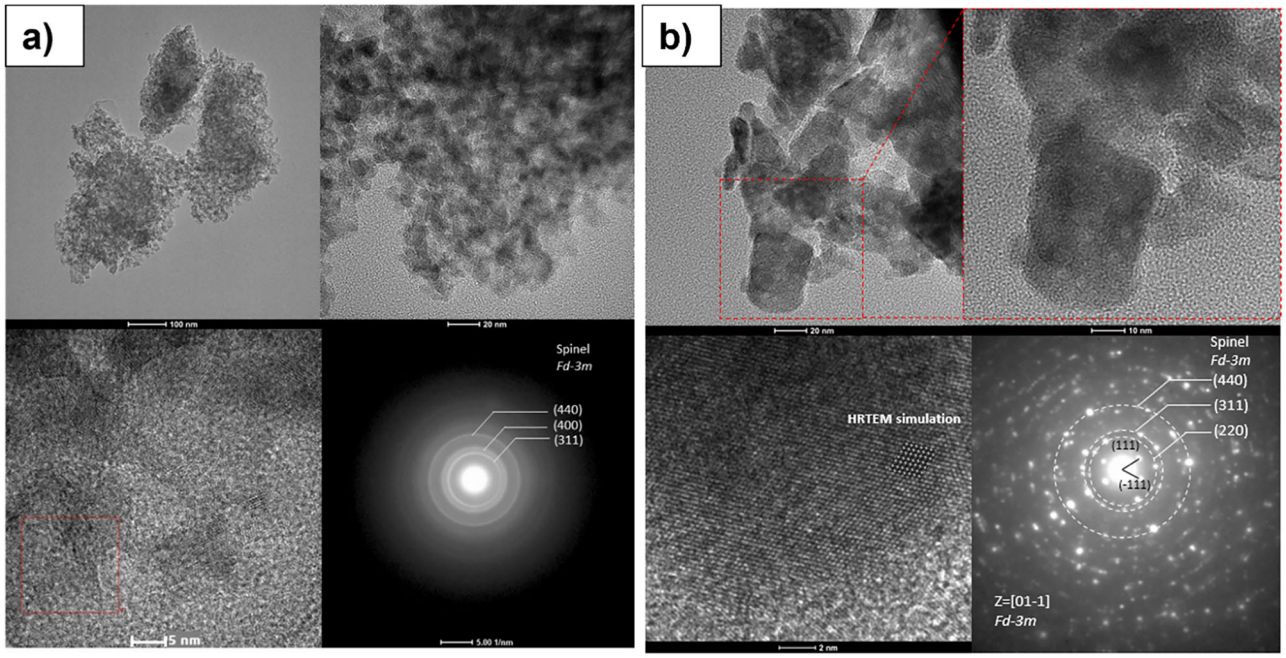

Fig. 10 TEM bright-field images: (**a**) MA support calcined at 800 °C, **b** NiCo-MA-800 fresh catalyst

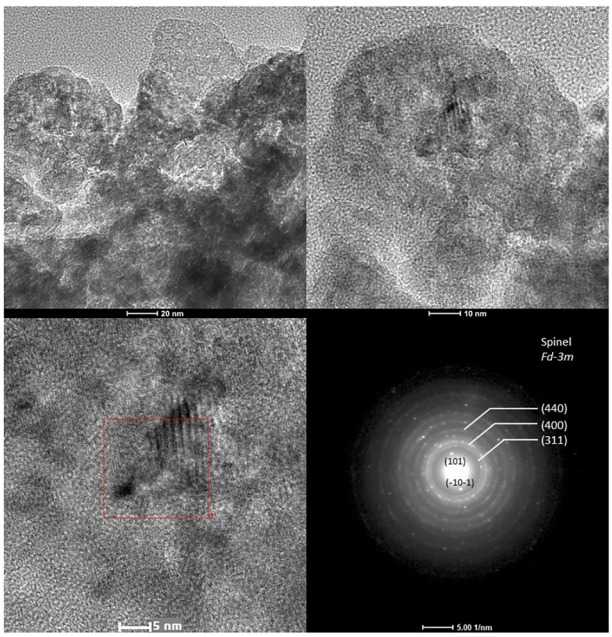

Fig. 11 TEM bright-field images of the NiCo-MA-800 spent catalyst

interfere with the detection of other phases, such as carbon. While the TEM analysis suggests the presence of amorphous carbon, the XRD analysis did not reveal distinct carbon or graphite peaks. This can be attributed to the amorphous nature of coke, which typically does not produce distinct diffraction peaks in XRD patterns.

The TEM-EDS mapping results (Online Resource Fig. S5) show the elemental distribution on the spent NiCo-MA catalyst. Mg, Al, O, Co, Ni, and Si are detected, with Si originating from the quartz mixed with the catalyst in a 1:1 volumetric ratio before loading into the reactor. The presence of C on the surface is attributed to coke formation during the reaction due to the CO_2 in the system. The uniform dispersion of Ni and Co suggests that the active phases are evenly distributed on the MA support and maintain their stability throughout the reaction. The good distribution of Ni and Co ions could be due to the nature of the spinel structure. Strong metal-support interaction due to the moderate surface basicity of Mg might allow a strong anchoring of Ni and Co ions, aiding homogeneity. Due to the structural stabilization preventing migration and agglomeration, Ni and Co active sites can be located in the same region. On the other hand, in the TEM or SEM images, it may not be possible to detect amorphous carbon in trace amounts, especially in the case of a spinel structure [67]. However, carbon formation in trace quantities has been verified by TGA results in which the mass loss for these samples ranged from 1.24% to 2.8%. The carbon was most likely to be amorphous in nature as confirmed by the oxidation of surface carbon at mild temperatures below 550 °C [50] and its low amounts may help to explain why carbon is not clearly visible in the TEM, SEM, or XRD analyses.

3.9 Hydrogen affinity (H2-TPR)

H_2-TPR studies were performed to monitor the reduction behavior of catalysts, and the results are shown in Fig. 12. The deconvoluted peaks in the Figure represent the stepwise

reduction processes of different metal oxides. The first peak (green) at around 350 °C corresponds to the reduction of Co_3O_4 to CoO, the second peak (blue) at around 410 °C is attributed to the reduction of CoO to Co, and the third peak (cyan) at above 450 °C represents the reduction of NiO to Ni [68–70]. These assignments are based on literature reports and the temperature shifts observed in the samples. Although the main reduction peak of NiO is above 450 °C, literature reports indicate that bulk NiO or NiO with weak support interactions can be reduced at 300–450 °C. This could contribute to the intensity of the CoO-to-Co reduction peak. However, this contribution is generally low; as an example it was reported to be 13% on Ni/γ-Al_2O_3 [71]. The reduction temperatures for Co_3O_4 to CoO and CoO to Co remained nearly constant for NiCo-MA-700 and NiCo-MA-800 catalysts with a significant peak shift in the third reduction step from 450 °C to 550 °C. However, a notable shift to higher temperatures was observed on NiCo-MA-900 for all reduction steps. It appears that increasing the calcination temperature modifies the surface structure of the support (i.e. its surface area, porosity and crystallinity) [72–75].

The reduction of Co_3O_4 follows the reactions outlined in reaction 4 and 5. In terms of H_2 consumption, the stoichiometry of the two-step Co reduction is 3:1 [76]. As given in Table 4, the Peak II/Peak I ratio represents the reducibility of Co species. The fact that NiCo-MA-800 has the closest value to the theoretical ratio suggests a fully reducible Co_3O_4 phase. However, the ratios for NiCo-MA-700 and NiCo-MA-900 deviate, with lower and higher values, respectively. This indicates that partial reduction occurs on NiCo-MA-700 leading to formation of $Co_{3-x}O_{4-y}$, whereas the higher H_2 consumption on NiCo-MA-900 suggests an increased reaction extent. Since the textural properties of MA support vary with thermal treatment, the interaction between the metal oxide species and the support also changes. As reported by Tomic-Tucakovic et al. [77], the calcination conditions of the Co catalyst and heating rate in H_2-TPR experiments significantly impact the reduction process altering the strength of metal oxide-support interactions, dispersion, crystal size and phases, metal oxide incorporation into the spinel lattice, etc. [78–80].

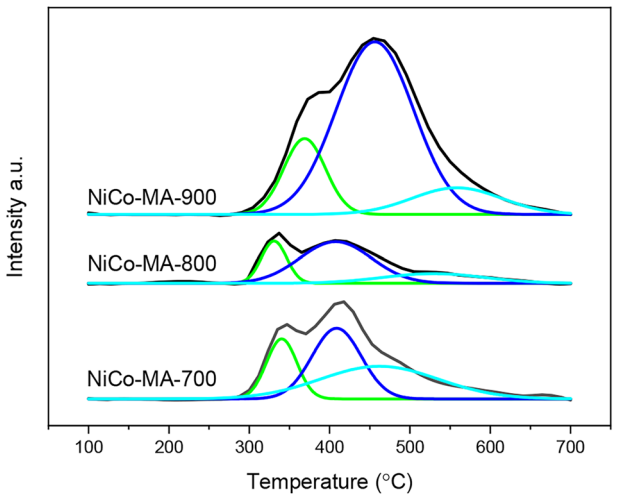

Fig. 12 H_2-TPR profiles of fresh catalysts

$$C_{o_3}O_4 + H_2 \rightarrow 3CoO + H_2O \quad (12)$$

$$3CoO + 3H_2 \rightarrow 3Co + 3H_2O \quad (13)$$

Plausibly, high calcination temperatures may promote strong metal-support interactions via the possible incorporation of Ni^{2+} or Co^{2+} ions into the spinel lattice, forming $(Ni,Mg)Al_2O_4$ or $(Co,Mg)Al_2O_4$. This might lead to structural stabilization of Ni and Co in octahedral or tetrahedral lattice positions. Consequently, the reduction would become more difficult due to the strong oxide bonding and lattice stabilization, shifting TPR peaks to higher temperatures as in the case of NiCo-MA-900. However, once activated at higher temperatures, metal oxides strongly bond to the spinel would consume more hydrogen per mole of metal due to multi-step reduction (e.g., $Co^{3+} \rightarrow Co^{2+} \rightarrow Co^0$). This might lead to an increase in TPR peak areas as a result of more reducing equivalents being consumed per mole of metal ion. At high temperatures, the support lattice itself may also contribute to H_2 consumption through the creation of oxygen vacancies [75, 77, 81].

3.10 Surface basicity (CO_2-TPD)

The surface basicity of the catalysts was investigated by CO_2-TPD experiments, as shown in Fig. 13. Since CO_2 acts

Table 4 H_2 Consumption and reduction behavior of NiCo-MA catalysts

Catalyst	H_2 consumption, (mmol/g active metal oxide)	Peak I (mmol/g active metal oxide)	Peak II (mmol/g active metal oxide)	Peak III (mmol/g active metal oxide)	Peak II/ Peak I
NiCo-MA-700	1.790	0.357	0.680	0.752	1.91
NiCo-MA-800	0.792	0.167	0.468	0.156	2.8
NiCo-MA-900	3.071	0.514	2.173	0.384	4.23

as a Lewis acid, the presence of basic sites on the catalyst promotes its adsorption. Higher basicity of the catalyst increases the CO_2 adsorption capacity and leads to higher CO_2 desorption at higher temperatures [70, 82]. Besides the total basicity of the catalyst, the type of basic sites also influences CO_2 methanation performance. In CO_2-TPD experiments, three distinct desorption regions are typically observed: low, moderate and high temperatures. At lower temperatures (100–150 °C), the observed peak is related to the weak basic sites, where CO_2 is physically adsorbed or loosely bound to surface hydroxyls. The medium basic sites, detected in the range of 150–350 °C, are primarily associated with surface oxygen anions (O^{2-}) and low-coordination Mg^{2+} ions acting as Lewis basic sites and surface –OH groups as Brønsted basic sites. At higher temperatures (350–600 °C), the strong basic sites are attributed to basic oxygen anions and the presence of coordinated lattice O^{2-} anions due to polydentate carbonate species [70, 83].

As can be observed in Fig. 13, increasing the calcination temperature of the support led to a shift of desorption peaks to higher temperatures. This indicates that CO_2 binding strength to the catalyst increased with support calcination temperature. The area under these peaks were calculated to determine the CO_2 desorption amount from each site. The

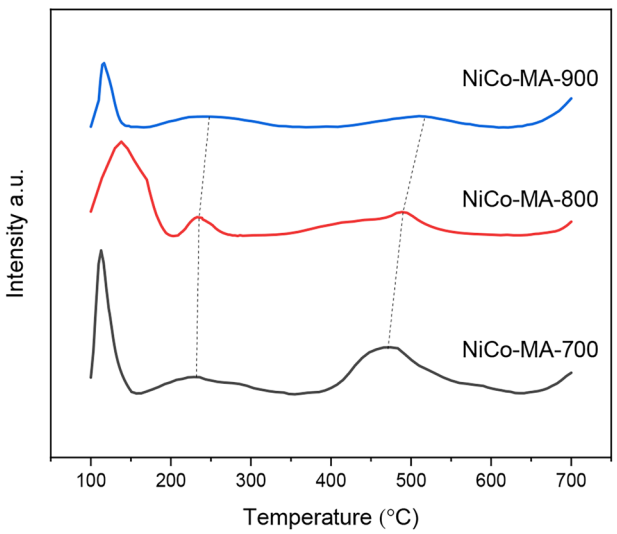

Fig. 13 CO_2-TPD profiles of NiCo-MA catalysts

individual and total CO_2 desorption amounts and the corresponding temperatures for weak, medium and strong basic sites are summarized in Table 5.

The effect of calcination temperature on the change of basicity has been elaborated by mechanistic interpretation. MA as a thermally stable mixed oxide with spinel structure exhibits inherent basicity due to its surface oxygen anions (O^{2-}) and low-coordination Mg^{2+} ions acting as Lewis basic sites and surface –OH groups as Brønsted basic sites. At high calcination temperatures, Ni^{2+} and Co^{2+} ions may be incorporated into the spinel lattice substituting Mg^{2+} or Al^{3+} ions and decreasing the available basic O^{2-} sites since oxygen ions become more structurally bound within the solid solution lattice. Besides, the loss of surface hydroxyl groups occurs through dehydroxylation reactions at elevated temperatures. Higher calcination temperatures result in a decrease in surface area, thereby reducing the number of accessible basic sites [84]. The total amount of desorbed CO_2 decreased with increasing calcination temperature of the support, consistent with the loss of BET surface area (Table 3). A higher surface area provides more accessible basic sites, which explains why NiCo-MA-700 exhibited the highest total desorption. However, it is notable that the weak basic sites were most abundant for NiCo-MA-800, suggesting that the distribution and strength of basic sites significantly varies with calcination temperature. The strength and number of basic sites on a catalytic surface should be well balanced [85] since too high-strength basic sites will passivate the active sites through the formation of highly stable surface carbonates while weak basic sites might not sufficiently polarize the CO_2 molecule for activation [86]. CO_2 adsorbed on weak basic sites is generally considered to desorb from the surface without reacting with H_2, thus having no effect on the methanation process [87]. During CO_2 adsorption, metal-O^{2-} pairs on the catalyst serves as medium-strength basic sites [88]. CO_2 adsorbed on the strong basic sites typically desorbs at temperatures far above 350 °C, meaning it does not directly contribute to the CO_2 methanation reaction at 350 °C [80]. However, an important observation is that the strong basic sites on NiCo-MA-800 began desorbing CO_2 at significantly lower temperatures, coinciding with the reaction temperature, compared to NiCo-MA-700 and NiCo-MA-900. This suggests that strong basic sites are still needed to break bonds or

Table 5 The amounts of CO_2 desorption on catalysts

Catalyst	T_{weak} (°C)	Weak basic site (mmol/gcat)	T_{medium} (°C)	Medium basic site (mmol/gcat)	T_{strong} (°C)	Strong basic site (mmol/gcat)	Total CO_2 desorption (mmol/gcat)
NiCo-MA-700	113	9.83	229	6.38	475	19.50	35.71
NiCo-MA-800	138	15.85	233	2.45	488	10.55	28.85
NiCo-MA-900	117	4.57	240	4.38	510	4.33	12.28

Table 6 Catalytic activity and product selectivity of the catalysts (Reaction condition: 350 °C, 1 bar, $H_2/CO = 4$, time on stream 21.5 h)

Catalyst	XCO_2, %	SCO, %	SCH_4, %	SC_2H_6, %	$Y_{CH4\ in\ gas}$, %	Coke formation[a], %	Y_{CH4}, (g CH_4 on C basis/g NiCo.s)	YCH_4, %
NiCo-MA-700	54.6	4.8	73.3	0.05	93.7	21.85	4.7	40
NiCo-MA-800	84.6	–	68.7	0.2	99.7	31.10	6.8	69
NiCo-MA-900	65.3	2.1	76.7	0.03	97.2	21.17	5.7	49

[a]Surface active C* species or amorphous carbon

stabilize reactive intermediates for CO_2 activation to enhance the methanation activity. When comparing the initial desorption temperatures of CO_2 from strong basic sites, the trend is as follows: NiCo-MA-800<NiCo-MA-900<NiCo-MA-700, which aligns well with the measured CO_2 conversion trend. These results highlight the need for an optimum number of medium to strength basic sites to activate CO_2 for dissociation into CO and O* that has been obtained for NiCo-MA-800.

3.11 Reaction analysis

The CO_2 methanation performance of the NiCo-MA catalysts, selected based on HT-CPA screening, was investigated at atmospheric pressure and 350 °C using a conventional reaction system. The results are summarized in Table 6 and illustrated in Figs. 14, 15. These results were calculated using Eqs. (1) to (7) for CO_2 conversion, CH_4 yield, and selectivity, revealing a clear correlation between the calcination temperature of the support and catalytic performance.

As shown in Fig. 14, NiCo-MA-800 exhibited the highest CO_2 conversion (~85%) with stable operation over 20 h. In contrast, NiCo-MA-700 demonstrated lower initial conversion, which further decreased over time. This decline in performance and evident deactivation can be attributed to weak structural stability and weaker metal-support interactions, as indicated by its lower reduction temperatures. This combination facilitates early activity but leads to sintering or carbon deposition, resulting in deactivation. NiCo-MA-900 displayed intermediate activity, maintaining stable conversion initially but showing a decline after 15 h of operation. The deactivation at longer times suggests possible sintering of active metal sites or carbon deposition [89].

The comparison of CO_2-TPD and catalytic performance data demonstrate a clear correlation between the distribution of basic sites and methanation activity. NiCo-MA-800, which exhibits the highest concentration of weak basic sites (15.85 mmol/gcat), also achieves the highest CO_2 conversion (84.6%) and methane yield (6.8 g CH_4/g NiCo.s), aligning with literature reports that weak basic sites

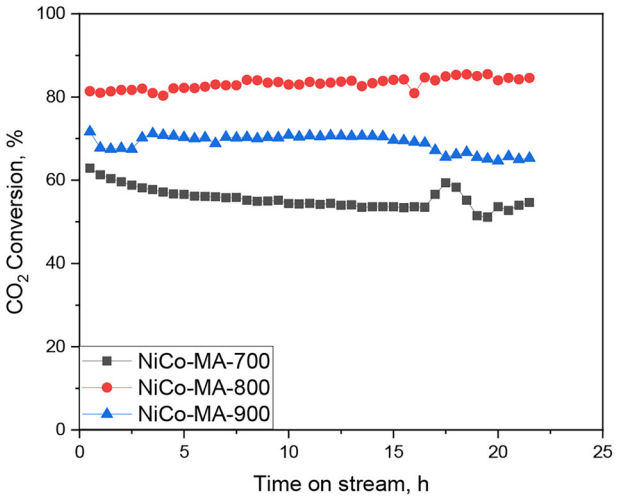

Fig. 14 Time on stream CO_2 conversion of NiCo-MA catalysts

facilitate CO_2 adsorption and activation. In contrast, NiCo-MA-700, despite having the highest strong basicity (19.50 mmol/gcat), shows lower CO_2 conversion (54.6%) and increased coke formation (21.85%), suggesting that excessive strong basicity can lead to over-adsorption of CO_2 and side reactions favoring carbon deposition. NiCo-MA-900, which has the lowest total CO_2 desorption capacity, exhibits moderate CO_2 conversion and methane yield, indicating that an optimal balance of weak and medium basic sites is crucial for maximizing methanation efficiency. These findings support previous studies emphasizing that strong basic sites alone do not necessarily enhance CO_2 methanation but rather require a well-balanced interaction between weak and medium basic sites to ensure efficient CO_2 activation and hydrogenation.

Figure 15 illustrates the CH_4 and CO selectivities of the catalysts, as well as CH_4 yields over time. NiCo-MA-800 achieved the most desirable performance, producing CH_4 as the sole gaseous product. Although its overall CH_4 selectivity was slightly lower than that of the other two catalysts, no detectable CO formation was observed, indicating minimal or no RWGS reaction. While NiCo-MA-700 and NiCo-MA-900 catalysts exhibited slightly higher CH_4 selectivity, significant amounts of CO were also detected.

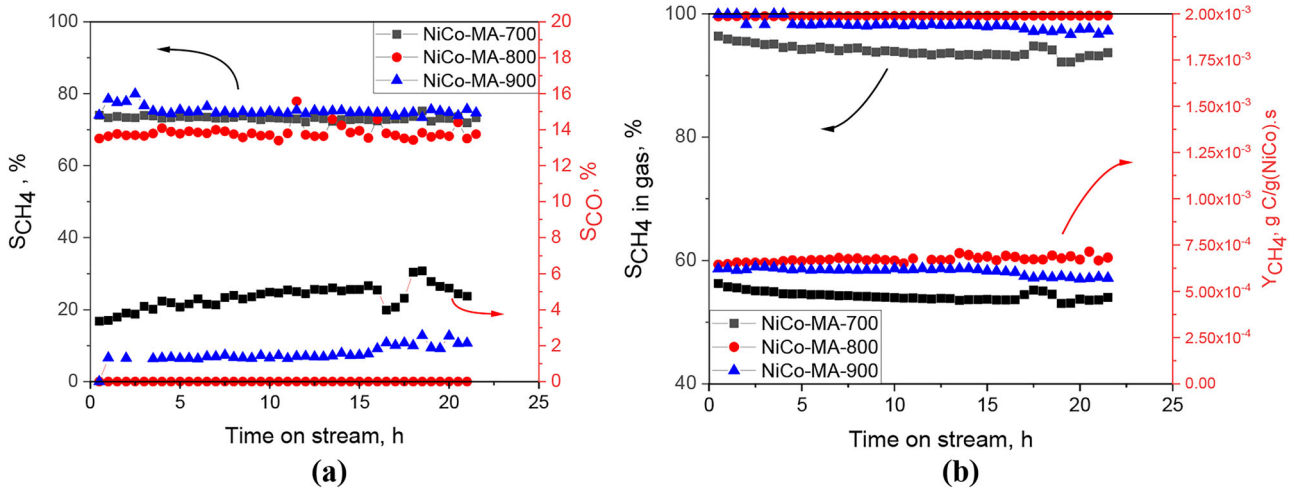

Fig. 15 Time on stream CH_4 and CO selectivities **a** and CH_4 yields **b** of the NiCo-MA catalysts

By individually assessing the performance of catalysts in conjunction with their characterization data, it can be concluded for NiCo-MA-700 catalyst that the high surface area (BET analysis) and lower reduction temperatures (TPR data) suggest that Ni and Co are more weakly bound to the support. This results in higher initial activity (relative to its final state) but poor stability. The high CO selectivity (Fig. 15a) and declining CH_4 selectivity over time (Fig. 15b) indicate the promotion of side reactions, such as RWGS, due to weak basic sites and lower reducibility. The superior performance of NiCo-MA-800 can be attributed to the optimal combination of moderate surface area, reducibility, and basicity. Strong basic sites on NiCo-MA-800, actively participating in CO_2 interaction at reaction temperatures (as confirmed by in CO_2-TPD experiments), facilitate CH_4 formation more efficiently than the other two catalysts at 350 °C. The CO_2-TPD data, combined with the reaction data, reveals that strong basic sites play a critical role in stabilizing intermediate carbonates essential for CH_4 formation. NiCo-MA-900 exhibited lower performance than NiCo-MA-800, likely due to excessive calcination, which reduced surface area and pore volume (as evidenced by N_2 physisorption analysis). This poor dispersion of Ni and Co oxides led to weaker catalytic performance. TPR data further revealed that NiO and Co_3O_4 reduction temperatures were higher for NiCo-MA-900, reflecting stronger metal-support interactions that may limit the availability of active metallic sites during the reaction. Additionally, a lower total CO_2 desorption amount in the TPD data supports this observation. The decline in CO_2 conversion for NiCo-MA-900 after 15 h suggests sintering or carbon deposition, a trend generally observed in catalysts with limited surface area [89].

It is widely accepted that medium-strength basic sites promote CO_2 methanation more effectively than strong basic sites, as excessively stable CO_2 adsorption can hinder reaction participation [87, 90]. While NiCo-MA-800 exhibits lower medium-strength basicity, its enhanced CO_2 activation at strong sites may follow alternative pathways, such as molecularly adsorbed CO_2 hydrogenation involving formate intermediates or CO dissociation pathways [59]. Liang et al. [91] conducted in-situ DRIFT studies during the methanation of CO_2 at the temperature of CO_2 desorption on weak basic sites of the reduced catalyst. According to the observed DRIFT bands, intermediates such as bicarbonate, formate and carbonate formed. With increasing reaction temperatures, bicarbonate intermediates diminished, while formate species increased. In our study, NiCo-MA-800 exhibited a higher density of weak basic sites, which are typically associated with surface hydroxyl groups or oxygen anions. These sites play a crucial role in adsorbing CO_2 and stabilizing it as bicarbonate (HCO_3^-) intermediates. The presence of these weak basic sites may promote the subsequent transformation of bicarbonate into formate ($HCOO^-$) intermediates, consistent with the mechanistic pathway proposed by Huynh et al. [92]. Based on medium basic site properties, the CO selectivity order follows: MA700 > MA900 > MA800. Further studies, such as in-situ spectroscopy, are necessary to confirm the exact reaction intermediates and pathways responsible for the observed behavior. In summary, NiCo-MA-800 emerges as the most effective catalyst due to its balance of reducibility, surface basicity, and stability. This combination enables high CO_2 conversion and CH_4 selectivity while minimizing side reactions and deactivation. These findings highlight the importance of optimizing the support calcination temperature to enhance catalyst the surface and structural properties for efficient and selective CO_2 methanation.

4 Conclusions

This study comprehensively evaluated the CO_2 methanation performance of MA spinel-supported catalysts prepared via

sol-gel processing and subsequently modified with Ni and Co. Thermodynamic analyses conducted using FactSage™ software confirmed the high-temperature stability of the MA spinel structure and illustrated the contributions of Ni and Co to phase stability. The oxidative resistance of Ni and the strong interaction of Co with the spinel phase enhanced the thermal stability of the catalysts, leading to significantly improved catalytic performance in CO_2 methanation. XRD and FT-IR analyses confirmed the formation of the MA spinel structure at 700 °C, with higher calcination temperatures improving crystallinity. However, calcination above 800 °C led to reduced surface area and pore volume due to sintering, which limited the homogeneous dispersion of Ni and Co and adversely affected catalytic performance. N_2 physisorption, H_2-TPR, and CO_2-TPD analyses demonstrated that NiCo-MA-800 provided the optimal balance between surface area, reducibility, and basicity, achieving the highest CO_2 conversion (~85%) and CH_4 selectivity among the catalysts tested. H_2-TPR results demonstrated that NiCo-MA-800 exhibited moderate metal-support interactions, with appropriate reduction temperatures for Ni and Co species. The strong basic sites identified in CO_2-TPD analysis further enhanced CO_2 activation and CH_4 formation at reaction temperatures, minimizing side reactions such as the RWGS reaction. Additionally, CO_2-TPD data revealed that despite the overall basicity decreased with increasing calcination temperature, NiCo-MA-800 maintained a favorable CO_2 desorption profile, facilitating enhanced CO_2 utilization.

Ni possessing high initial hydrogenation activity would come predominantly from its weak metal-support interaction by impregnation and mild calcination. However, some of the Ni was potentially embedded into the spinel lattice at high calcination temperatures and reduction conditions. This may lead to the formation of partially reduced spinel to stabilize Ni particles from sintering and coke deposition, which still act catalytically as well. On the other hand, Co tends to segregate more readily and form separate oxides or metallic phases as indicated by its retained TPR profiles even at high calcination temperatures. Calcination also appeared to adjust the overall basic site number and strengths as demonstrated by TPD measurements. In conclusion, NiCo-MA-800 emerged as the most effective catalyst, providing superior CO_2 conversion, CH_4 selectivity, and stability, owing to its optimized structural and surface properties. It has been shown that long-term stability can be imparted to Ni, an excellent metal for hydrogenation, via incorporation into $MgAl_2O_4$ spinel and with the chosen high calcination conditions. Moreover, its low oxygen affinity can be tolerated by use of a bimetallic system, preferably employing Co.

This work highlights the crucial role of calcination temperature in tuning catalytic performance and emphasizes the importance of strong basic sites in facilitating CO_2 activation and CH_4 formation. Future research should focus on mitigating carbon deposition and further investigating reaction mechanisms through in-situ spectroscopic techniques to improve catalyst stability and efficiency.

Data availability

No datasets were generated or analysed during the current study.

Supplementary information The online version contains supplementary material available at https://doi.org/10.1007/s10971-025-06799-1.

Acknowledgements We would like to acknowledge the Istanbul Technical University Scientific Research Projects Funding (ITU-BAP) (Projects No: 43781 and 43596) for their financial support. Duygu Yeşiltepe-Özçelik would like to thank her gratitude to the Tinçel Culture Foundation to providing research fellowships that enabled 3 months stay at Department of Chemistry and Chemical Engineering, Chalmers University of Technology, Gothenburg, Sweden.

Author contributions DY.Ö: conceptualization, investigation, methodology, formal analysis, writing—original draft. UB: methodology, writing review and editing, formal analysis. FK: writing, data curation, formal analysis. EU: data curation, formal analysis. BD: formal analysis, conceptualization, software. AS: data curation, formal analysis. PAC: supervision, formal analysis. GGG: supervision, writing review and editing, formal analysis. AS: supervision, formal analysis. SG: supervision, formal analysis. All authors reviewed the manuscript.

Funding Open access funding provided by the Scientific and Technological Research Council of Türkiye (TÜBİTAK).

Compliance with ethical standards

Conflict of interest The authors declare no competing interests.

Publisher's note Springer Nature remains neutral with regard to jurisdictional claims in published maps and institutional affiliations.

Open Access This article is licensed under a Creative Commons Attribution 4.0 International License, which permits use, sharing, adaptation, distribution and reproduction in any medium or format, as long as you give appropriate credit to the original author(s) and the source, provide a link to the Creative Commons licence, and indicate if changes were made. The images or other third party material in this article are included in the article's Creative Commons licence, unless indicated otherwise in a credit line to the material. If material is not included in the article's Creative Commons licence and your intended use is not permitted by statutory regulation or exceeds the permitted use, you will need to obtain permission directly from the copyright holder. To view a copy of this licence, visit http://creativecommons.org/licenses/by/4.0/.

References

1. Orege JI, Kifle GA, Yu Y, Wei J, Ge Q, Sun J (2023) Emerging spinel ferrite catalysts for driving CO2 hydrogenation to high-value chemicals. Matter 6:1404–1434. https://doi.org/10.1016/j.matt.2023.03.024

2. Weber D, Wadlinger KM, Heinlein MM, Franken T (2022) Modifying spinel precursors for highly active and stable Ni-based CO2 methanation catalysts. ChemCatChem 14:1–7. https://doi.org/10.1002/cctc.202200563
3. Navarro JC, Hurtado C, Gonzalez-Castaño M, Bobadilla LF, Ivanova S, Cumbrera FL, Centeno MA, Odriozola JA (2023) Spinel ferrite catalysts for CO2reduction via reverse water gas shift reaction. J CO2 Util 68:2–7. https://doi.org/10.1016/j.jcou.2022.102356
4. Orege JI, Wei J, Ge Q, Sun J (2023) Spinel-structured nanocatalysts: New opportunities for CO2 hydrogenation to value-added chemicals. Nano Today 51:101914. https://doi.org/10.1016/j.nantod.2023.101914
5. Lee H, Calvin K, Dasgupta D, Krinner G, Mukherji A, Thorne P, Trisos C, Romero J, Aldunce P (2022) IPCC Sixth Assessment Report - Synthesis Report.
6. Memon MA, Jiang Y, Hassan MA, Ajmal M, Wang H, Liu Y (2023) Heterogeneous Catalysts for Carbon Dioxide Methanation: A View on Catalytic Performance. Catalysts 13:1–24. https://doi.org/10.3390/catal13121514
7. Sun H, Sun S, Liu T, Zeng J, Wang Y, Yan Z, Wu C (2024) Integrated CO2 capture and utilization: Selection, matching, and interactions between adsorption and catalytic sites. ACS Catal 15572–15589. https://doi.org/10.1021/acscatal.4c03861.
8. Tommasi M, Degerli SN, Ramis G, Rossetti I (2024) Advancements in CO2 methanation: A comprehensive review of catalysis, reactor design and process optimization. Chem Eng Res Des 201:457–482. https://doi.org/10.1016/j.cherd.2023.11.060
9. Hervy M, Maistrello J, Brito L, Rizand M, Basset E, Kara Y, Maheut M (2021) Power-to-gas: CO2 methanation in a catalytic fluidized bed reactor at demonstration scale, experimental results and simulation. J CO2 Util 50:101610. https://doi.org/10.1016/j.jcou.2021.101610
10. Kakoee A, Gharehghani A (2020) Carbon oxides methanation in equilibrium; a thermodynamic approach. Int J Hydrog Energy 45:29993–30008. https://doi.org/10.1016/j.ijhydene.2020.08.073
11. Salmi C, Zelca Z, Laouini SE, Meneceur S, Mohammed HA, Abdullah JAA, Abdullah, MMS (2024) Gallic acid assisted synthesis of novel CuO/Ni/Fe3O4 nanocomposite for catalytic CO2 methanation and photocatalytic hydrogen generation, J. Sol-Gel Sci. Technol. https://doi.org/10.1007/s10971-024-06608-1.
12. Kim DH, Youn JR, Seo JC, Kim SB, Kim MJ, Lee K (2023) One-pot synthesis of NiCo/MgAl2O4 catalyst for high coke-resistance in steam methane reforming: Optimization of Ni/Co ratio. Catal Today 411–412:113910. https://doi.org/10.1016/j.cattod.2022.09.016
13. Stangeland K, Kalai D, Li H, Yu Z (2017) CO2 methanation: The effect of catalysts and reaction conditions. Energy Procedia 105:2022–2027. https://doi.org/10.1016/j.egypro.2017.03.577
14. Wang Y, Arandiyan H, Scott J, Bagheri A, Dai H, Amal R (2017) Recent advances in ordered meso/macroporous metal oxides for heterogeneous catalysis: A review. J Mater Chem A 5:8825–8846. https://doi.org/10.1039/c6ta10896b
15. Azancot L, Bobadilla LF, Centeno MA, Odriozola JA (2021) IR spectroscopic insights into the coking-resistance effect of potassium on nickel-based catalyst during dry reforming of methane, Appl Catal. B Environ 285. https://doi.org/10.1016/j.apcatb.2020.119822.
16. Tada S, Ochieng OJ, Kikuchi R, Haneda T, Kameyama H (2014) Promotion of CO2 methanation activity and CH4 selectivity at low temperatures over Ru/CeO2/Al2O 3 catalysts. Int J Hydrog Energy 39:10090–10100. https://doi.org/10.1016/j.ijhydene.2014.04.133
17. Li T, Wang S, Gao DN, Wang SD (2014) Effect of support calcination temperature on the catalytic properties of Ru/Ce0.8Zr0.2O2 for methanation of carbon dioxide, Ranliao Huaxue Xuebao/. J Fuel Chem Technol 42:1440–1446. https://doi.org/10.1016/s1872-5813(15)60001-9
18. Garbarino G, Bellotti D, Riani P, Magistri L, Busca G (2015) Methanation of carbon dioxide on Ru/Al2O3 and Ni/Al2O3 catalysts at atmospheric pressure: Catalysts activation, behaviour and stability. Int J Hydrog Energy 40:9171–9182. https://doi.org/10.1016/j.ijhydene.2015.05.059
19. Ma Y, Liu J, Chu M, Yue J, Cui Y, Xu G (2022) Enhanced low-temperature activity of CO2 methanation over Ni/CeO2 catalyst. Catal Lett 152:872–882. https://doi.org/10.1007/s10562-021-03677-7
20. Tsiotsias AI, Charisiou ND, Italiano C, Ferrante GD, Pino L, Vita A, Sebastian V, Hinder SJ, Baker MA, Sharan A, Singh N, Polychronopoulou K, Goula MA (2024) Ni-noble metal bimetallic catalysts for improved low temperature CO2 methanation. Appl Surf Sci 646:158945. https://doi.org/10.1016/j.apsusc.2023.158945
21. Vrijburg WL, Moioli E, Chen W, Zhang M, Terlingen BJP, Zijlstra B, Filot IAW, Züttel A, Pidko EA, Hensen EJM (2019) Efficient Base-Metal NiMn/TiO2 Catalyst for CO2 Methanation. ACS Catal 9:7823–7839. https://doi.org/10.1021/acscatal.9b01968
22. Ridzuan NDM, Shaharun MS, Anawar MA, Ud-Din I (2022) Ni-based catalyst for carbon dioxide methanation: A review. Catalysts 12:469
23. Cai M, Wen J, Chu W, Cheng X, Li Z (2011) Methanation of carbon dioxide on Ni/ZrO2-Al2O 3 catalysts: Effects of ZrO2 promoter and preparation method of novel ZrO2-Al2O3 carrier. J Nat Gas Chem 20:318–324. https://doi.org/10.1016/S1003-9953(10)60187-9
24. Ren J, Qin X, Yang JZ, Qin ZF, Guo HL, Lin JY, Li Z (2015) Methanation of carbon dioxide over Ni-M/ZrO2 (M = Fe, Co, Cu) catalysts: Effect of addition of a second metal,. Fuel Process Technol 137:204–211. https://doi.org/10.1016/j.fuproc.2015.04.022
25. Bartholomew CH, Weatherbee GD, Jarvi GA (1980) Effects of carbon deposits on the specific activity of nickel and nickel bimetallic catalysts. Chem Eng Commun 5:125–134. https://doi.org/10.1080/00986448008935959
26. Ma S, Tan Y, Han Y (2011) Methanation of syngas over coral reef-like Ni/Al2O3 catalysts. J Nat Gas Chem 20:435–440. https://doi.org/10.1016/S1003-9953(10)60192-2
27. Sanjabi S, Obeydavi A (2015) Synthesis and characterization of nanocrystalline MgAl2O4 spinel via modified sol-gel method. J Alloy Compd 645:535–540. https://doi.org/10.1016/j.jallcom.2015.05.107
28. Saberi A, Golestani-Fard F, Sarpoolaky H, Willert-Porada M, Gerdes T, Simon R (2008) Chemical synthesis of nanocrystalline magnesium aluminate spinel via nitrate-citrate combustion route. J Alloy Compd 462:142–146. https://doi.org/10.1016/j.jallcom.2007.07.101
29. Neri G, Rizzo G, Galvagno S, Loiacono G, Donato A, Musolino MG, Pietropaolo R, Rombi E (2004) Sol-gel synthesis, characterization and catalytic properties of Fe-Ti mixed oxides. Appl Catal A Gen 274:243–251. https://doi.org/10.1016/j.apcata.2004.07.007
30. Rahmat N, Yaakob Z, Pudukudy M, Rahman NA, Jahaya SS (2018) Single step solid-state fusion for MgAl2O4 spinel synthesis and its influence on the structural and textural properties. Powder Technol 329:409–419. https://doi.org/10.1016/j.powtec.2018.02.007
31. Bush AJ, Beyer R, Trautman R, Barbé CJ, Bartlett JR (2004) Ceramic micro-particles synthesised using emulsion and sol-gel technology: An investigation into the controlled release of encapsulants and the tailoring of micro-particle size. J Sol-Gel Sci Technol 32:85–90. https://doi.org/10.1007/s10971-004-5770-z
32. Shilova OA, Kovalenko AS, Nikolaev AM, Mjakin SV, Sinel'nikov AA, Chelibanov VP, Gorshkova YE, Tsvigun NV,

Ruzimuradov ON, Kopitsa GP (2023) Surface and photocatalytic properties of sol–gel derived TiO2@SiO2 core-shell nanoparticles. J Sol-Gel Sci Technol 108:263–273. https://doi.org/10.1007/s10971-022-05943-5
33. Habibi N, Wang Y, Arandiyan H, Rezaei M (2017) Low-temperature synthesis of mesoporous nanocrystalline magnesium aluminate (MgAl2O4) spinel with high surface area using a novel modified sol-gel method. Adv Powder Technol 28:1249–1257. https://doi.org/10.1016/j.apt.2017.02.012
34. Burgun U, Zonouz HR, Okutan H, Atakül H, Senkan S, Sarioglan A, Gur GG (2023) Effects of rare earth metal promotion over zeolite-supported Fe−Cu-based catalysts on the light olefin production performance in Fischer−Tropsch synthesis. ACS Omega 8:648–662. https://doi.org/10.1021/acsomega.2c05795
35. Wen Y, Liu X, Chen X, Jia Q, Yu R, Ma T (2017) Effect of heat treatment conditions on the growth of MgAl2O4 nanoparticles obtained by sol-gel method. Ceram Int 43:15246–15253. https://doi.org/10.1016/j.ceramint.2017.08.061
36. Almirón Baca J, Alcázar Rojas H, Churata Añasco R, Vargas Vilca M, Alcázar Rojas L, Fim F (2018) Synthesis of ni-cu catalysts by impregnation to obtain carbon nanofibers by catalytic decomposition of methane, Rev. La Soc. Química Del Perú 84:91–196
37. Wang Y, Peng J, Zhou C, Lim ZY, Wu C, Ye S, Wang WG (2014) Effect of Pr addition on the properties of Ni/Al2O3 catalysts with an application in the autothermal reforming of methane. Int J Hydrog Energy 39:778–787. https://doi.org/10.1016/j.ijhydene.2013.10.071
38. Munnik P, De Jongh PE, De Jong KP (2015) Recent developments in the synthesis of supported catalysts. Chem Rev 115:6687–6718. https://doi.org/10.1021/cr500486u
39. Valinejad Moghaddam S, Rezaei M, Meshkani F, Daroughegi R (2018) Carbon dioxide methanation over Ni-M/Al2O3 (M: Fe, CO, Zr, La and Cu) catalysts synthesized using the one-pot sol-gel synthesis method. Int J Hydrog Energy 43:16522–16533. https://doi.org/10.1016/j.ijhydene.2018.07.013
40. Tsiotsias AI, Charisiou ND, Yentekakis IV, Goula MA (2021) Bimetallic ni-based catalysts for co2 methanation: A review. Nanomaterials 11:1–34. https://doi.org/10.3390/nano11010028
41. Qin Z, Zhou Y, Jiang Y, Liu Z, Ji H (2017) Recent advances in heterogeneous catalytic hydrogenation of CO2 to methane. New Adv Hydrog Process - Fundam Appl. https://doi.org/10.5772/65407.
42. Hwang S, Lee J, Hong UG, Baik JH, Koh DJ, Lim H, Song IK (2013) Methanation of carbon dioxide over mesoporous Ni-Fe-Ru-Al2O3 xerogel catalysts: Effect of ruthenium content. J Ind Eng Chem 19:698–703. https://doi.org/10.1016/j.jiec.2012.10.007
43. Gür GG, Atik Ö (2022) Effect of promoter type and synthesis method on catalytic performance of Fe-Mn based FT-olefin catalysts. Turk J Chem 46:941–955. https://doi.org/10.55730/1300-0527.3406
44. Ho SW, Su YS (1997) Effects of ethanol impregnation on the properties of silica-supported cobalt catalysts. J Catal 168:51–59. https://doi.org/10.1006/jcat.1997.1614
45. Bale CW, Bélisle E, Chartrand P, Decterov SA, Eriksson G, Gheribi AE, Hack K, Jung IH, Kang YB, Melançon J, Pelton AD, Petersen S, Robelin C, Sangster J, Spencer P, Van Ende MA (2016) FactSage thermochemical software and databases, 2010-2016. Calphad Comput Coupling Phase Diagr Thermochem 54:35–53. https://doi.org/10.1016/j.calphad.2016.05.002
46. Chen S, Hu YH (2025) Progress in the development of NiO/MgO solid solution catalysts: A review. Surf Innov 13:84–94. https://doi.org/10.1680/jsuin.24.00103
47. Dash S, Sahoo RK, Das A, Bajpai S, Debasish D, Singh SK (2017) Synthesis of MgAl2O4 spinel by thermal plasma and its synergetic structural study. J Alloy Compd 726:1186–1194. https://doi.org/10.1016/j.jallcom.2017.08.085
48. Pastor-Pérez L, Patel V, Le Saché E, Reina TR (2020) CO2 methanation in the presence of methane: Catalysts design and effect of methane concentration in the reaction mixture. J Energy Inst 93:415–424. https://doi.org/10.1016/j.joei.2019.01.015
49. Aramouni NAK, Zeaiter J, Kwapinski W, Leahy JJ, Ahmad MN (2021) Trimetallic Ni-Co-Ru catalyst for the dry reforming of methane: Effect of the Ni/Co ratio and the calcination temperature. Fuel 300. https://doi.org/10.1016/j.fuel.2021.120950.
50. Owen RE, Zhang YS, Neville TP, Manos G, Shearing PR, Brett DJL, Bailey JJ (2022) Visualising coke-induced degradation of catalysts used for CO2-reforming of methane with X-ray nano-computed tomography, Carbon Capture Sci Technol 5. https://doi.org/10.1016/j.ccst.2022.100068.
51. Lukong VT, Chukwuati CN, Ukoba K, Jen TC (2023) The role of calcination temperature in the self-cleaning functionality of urea-doped TiO2 prepared through in situ heat-assisted sol–gel synthesis. J Mater Eng Perform 32:11143–11156. https://doi.org/10.1007/s11665-023-08727-2
52. Phromma S, Wutikhun T, Kasamechonchung P, Eksangsri T, Sapcharoenkun C (2020) Effect of calcination temperature on photocatalytic activity of synthesized TiO2 nanoparticles via wet ball milling sol-gel method, Appl Sci 10 (2020). https://doi.org/10.3390/app10030993.
53. Ganesh I (2013) A review on magnesium aluminate (MgAl2O4) spinel: Synthesis, processing and applications,. Int Mater Rev 58:63–112. https://doi.org/10.1179/1743280412Y.0000000001
54. Carvalho LS, de Melo VR, e Melo EV, Sobrinho D, Ruiz DM, de Araújo Meloa (2018) Effect of urea excess on the properties of the MgAl2O4 obtained by microwave-assisted combustion. Mater Res 21:1–11. https://doi.org/10.1590/1980-5373-MR-2017-0189
55. Liu S, Chen C, Liu Q, Zhuo Y, Yuan D, Dai Z, Bao J (2015) Two-dimensional porous γ-AlOOH and γ-Al2O3 nanosheets: Hydrothermal synthesis, formation mechanism and catalytic performance. RSC Adv 5:71728–71734. https://doi.org/10.1039/c5ra09772j
56. Aalam CS, Saravanan CG, Kannan M (2015) Experimental investigations on a CRDI system assisted diesel engine fuelled with aluminium oxide nanoparticles blended biodiesel. Alex Eng J 54:351–358. https://doi.org/10.1016/j.aej.2015.04.009
57. Zahir MH, Rahman MM, Irshad K, Rahman MM (2019) Shape-stabilized phase change materials for solar energy storage: MgO and mg(OH)2 mixed with polyethylene glycol. Nanomaterials 9:1–21. https://doi.org/10.3390/nano9121773
58. Guo J, Lou H, Zhao H, Wang X, Zheng X (2004) Novel synthesis of high surface area MgAl2O4 spinel as catalyst support. Mater Lett 58:1920–1923. https://doi.org/10.1016/j.matlet.2003.12.013
59. Kim J (2024) Ni catalysts for thermochemical CO2 methanation: A review, Coatings 14. https://doi.org/10.3390/coatings14101322.
60. Dhak D, Pramanik P (2006) Particle size comparison of soft-chemically prepared transition metal (Co, Ni, Cu, Zn) aluminate pinels. J Am Ceram Soc 89:1014–1021. https://doi.org/10.1111/j.1551-2916.2005.00769.x
61. Goodwin JG, Blackmond DG, Lester JE (1982) Application of fourier transform infrared spectroscopy to studies of coke formation on cracking catalysts. https://doi.org/10.1007/978-94-009-7597-2_7.
62. Devaraj A, Vijayakumar M, Bao J, Guo MF, Derewinski MA, Xu Z, Gray MJ, Prodinger S, Ramasamy KK (2016) Discerning the Location and Nature of Coke Deposition from Surface to Bulk of Spent Zeolite Catalysts. Sci Rep. 6:1–11. https://doi.org/10.1038/srep37586
63. Deka DJ, Kim J, Gunduz S, Jain D, Shi Y, Miller JT, Co AC, Ozkan US (2021) Coke formation during high-temperature CO2 electrolysis over AFeO3 (A = La/Sr) cathode: Effect of A-site metal segregation. Appl Catal B Environ 283:119642. https://doi.org/10.1016/j.apcatb.2020.119642

64. Vinila VS, Isac J. Synthesis and structural studies of superconducting perovskite GdBa2Ca3Cu4O10.5+d nanosystems, Elsevier Inc., 2021. https://doi.org/10.1016/B978-0-12-820558-7.00022-4.
65. Sundaresan A, Rao CNR (2009) Ferromagnetism as a universal feature of inorganic nanoparticles. Nano Today 4:96–106. https://doi.org/10.1016/j.nantod.2008.10.002
66. Azalim S, Brahmi R, Bensitel M, Giraudon JM, Lamonier JF (2010) Preparation and characterization of nanocrystallines Mn-Ce-Zr mixed oxide catalysts by sol-gel method: Application to the complete oxidation of n-butanol, Elsevier Masson SAS. https://doi.org/10.1016/S0167-2991(10)75147-8.
67. Katheria S, Gupta A, Deo G, Kunzru D (2016) Effect of calcination temperature on stability and activity of Ni/MgAl2O4 catalyst for steam reforming of methane at high pressure condition. Int J Hydrog Energy 41:14123–14132. https://doi.org/10.1016/j.ijhydene.2016.05.109
68. Ji Y, Zhao Z, Duan A, Jiang G, Liu J (2009) Comparative study on the formation and reduction of bulk and Al 2O3-supported cobalt oxides by H2-TPR technique. J Phys Chem C 113:7186–7199. https://doi.org/10.1021/jp8107057
69. Lim TH, Cho SJ, Yang HS, Engelhard MH, Kim DH (2015) Effect of Co/Ni ratios in cobalt nickel mixed oxide catalysts on methane combustion. Appl Catal A Gen 505:62–69. https://doi.org/10.1016/j.apcata.2015.07.040
70. Andache M, Rezaei M, Taherkhani Z (2021) Steam reforming for syngas production over Ni and Ni-promoted catalysts. Res Chem Intermed 47:3661–3672. https://doi.org/10.1007/s11164-021-04493-9
71. Cho JH, An SH, Chang TS, Shin CH (2016) Effect of an alumina phase on the reductive amination of 2-propanol to monoisopropylamine over Ni/Al2O3. Catal Lett 146:811–819. https://doi.org/10.1007/s10562-016-1695-8
72. Berent K, Komarek S, Lach R, Pyda W (2019) The effect of calcination temperature on the structure and performance of nanocrystalline mayenite powders, Materials (Basel). 12. https://doi.org/10.3390/ma12213476.
73. Márquez G, Sagredo V, Guillén-Guillén R, Attolini G, Bolzoni F (2020) Calcination effects on the crystal structure and magnetic properties of CoFe2O4 nanopowders synthesized by the coprecipitation method. Rev Mex Fis 66:251–257. https://doi.org/10.31349/REVMEXFIS.66.251
74. Silva JB, De Brito W, Mohallem NDS (2004) Influence of heat treatment on cobalt ferrite ceramic powders. Mater Sci Eng B 112:182–187. https://doi.org/10.1016/j.mseb.2004.05.029
75. Pandey D, Deo G (2016) Effect of support on the catalytic activity of supported Ni-Fe catalysts for the CO2 methanation reaction. J Ind Eng Chem 33:99–107. https://doi.org/10.1016/j.jiec.2015.09.019
76. Lin HY, Chen YW (2004) The mechanism of reduction of cobalt by hydrogen. Mater Chem Phys 85:171–175. https://doi.org/10.1016/j.matchemphys.2003.12.028
77. Tomić-Tucaković B, Majstorović D, Jelić D, Mentus S (2012) Thermogravimetric study of the kinetics of Co 3O 4 reduction by hydrogen. Thermochim Acta 541:15–24. https://doi.org/10.1016/j.tca.2012.04.018
78. Madduluri VR, Nagaiah P, Prathap C, Vasikerappa K, Nagu A, David Raju B, Rama Rao KS (2020) Synergistic interface between Co3O4 and MgAl2O4 in CO2 assisted continuous vapour phase oxidative dehydrogenation of ethylbenzene to styrene monomer. Arab J Chem 13:2883–2896. https://doi.org/10.1016/j.arabjc.2018.07.018
79. Alrafei B, Polaert I, Ledoux A, Azzolina-Jury F (2020) Remarkably stable and efficient Ni and Ni-Co catalysts for CO2 methanation. Catal Today 346:23–33. https://doi.org/10.1016/j.cattod.2019.03.026
80. Mebrahtu C, Krebs F, Abate S, Perathoner S, Centi G, Palkovits R (2019) CO2 methanation: Principles and challenges, 1st ed., Elsevier B.V. https://doi.org/10.1016/B978-0-444-64127-4.00005-7.
81. Kim DH, Youn JR, Seo JC, Kim SB, Kim MJ, Lee K (2023) One-pot synthesis of NiCo/MgAl2O4 catalyst for high coke-resistance in steam methane reforming: Optimization of Ni/Co ratio. Catal. Today 411–412. https://doi.org/10.1016/j.cattod.2022.09.016.
82. Summa P, Świrk Da Costa K, Gopakumar J, Samojeden B, Motak M, Rønning M, Van Beek W, Da Costa P (2023) Optimization of Co-Ni-Mg-Al mixed-oxides CO2 methanation catalysts with solution combustion synthesis: On the importance of Co incorporation and basicity. Appl Mater Today 32. https://doi.org/10.1016/j.apmt.2023.101795.
83. Dębek R, Motak M, Galvez ME, Grzybek T, Da Costa P (2018) Promotion effect of zirconia on Mg(Ni,Al)O mixed oxides derived from hydrotalcites in CO2 methane reforming. Appl Catal B Environ 223:36–46. https://doi.org/10.1016/j.apcatb.2017.06.024
84. Abdulrasheed A, Jalil AA, Gambo Y, Ibrahim M, Hambali HU, Shahul Hamid MY (2019) A review on catalyst development for dry reforming of methane to syngas: Recent advances. Renew Sustain Energy Rev 108:175–193. https://doi.org/10.1016/j.rser.2019.03.054
85. Aziz MAA, Jalil AA, Wongsakulphasatch S, Vo DVN (2020) Understanding the role of surface basic sites of catalysts in CO2 activation in dry reforming of methane: A short review. Catal Sci Technol 10:35–45. https://doi.org/10.1039/c9cy01519a
86. Molinet-Chinaglia C, Shafiq S, Serp P (2024) Low temperature sabatier CO2 methanation, ChemCatChem 16. https://doi.org/10.1002/cctc.202401213.
87. Gao X, Wang Z, Huang Q, Jiang M, Askari S, Dewangan N, Kawi S (2022) State-of-art modifications of heterogeneous catalysts for CO2 methanation – Active sites, surface basicity and oxygen defects. Catal Today 402:88–103. https://doi.org/10.1016/j.cattod.2022.03.017
88. Italiano C, Llorca J, Pino L, Ferraro M, Antonucci V, Vita A (2020) CO and CO2 methanation over Ni catalysts supported on CeO2, Al2O3 and Y2O3 oxides. Appl Catal B Environ 264:118494. https://doi.org/10.1016/j.apcatb.2019.118494
89. Kim DH, Seo JC, Kim YJ, Kim J, Yoon S, Ra H, Kim MJ, Lee K (2024) Ni-Co alloy catalyst derived from NixCoy/MgAl2O4 via exsolution method for high coke resistance toward dry reforming of methane. Catal Today 425:114337. https://doi.org/10.1016/j.cattod.2023.114337
90. Li Z, Chen J, Xie Y, Wen J, Weng H, Wang M, Zhang J, Cao J, Tian G, Zhang Q, Ning P (2024) Zonal activation of molecular carbon dioxide and hydrogen over dual sites Ni-Co-MgO catalyst for CO2 methanation: Synergistic catalysis of Ni and Co species. J Energy Chem 91:213–225. https://doi.org/10.1016/j.jechem.2023.12.027
91. Liang C, Ye Z, Dong D, Zhang S, Liu Q, Chen G, Li C, Wang Y, Hu X (2019) Methanation of CO2: Impacts of modifying nickel catalysts with variable-valence additives on reaction mechanism. Fuel 254:115654. https://doi.org/10.1016/j.fuel.2019.115654
92. Huynh HL, Zhu J, Zhang G, Shen Y, Tucho WM, Ding Y, Yu Z (2020) Promoting effect of Fe on supported Ni catalysts in CO2 methanation by in situ DRIFTS and DFT study. J Catal 392:266–277. https://doi.org/10.1016/j.jcat.2020.10.018